Aeroelastic Control and Estimation with a Minimal Nonlinear Modal Description

Marc Artola [*], Norberto Goizueta[†], Andrew Wynn [‡] and Rafael Palacios [§]
Department of Aeronautics, Imperial College London, London, UK, SW7 2AZ

Modal-based, nonlinear Moving Horizon Estimation (MHE) and Model Predictive Control (MPC) strategies for very flexible aeroelastic systems are presented. They are underpinned by an aeroelastic model built from a 1D intrinsic (based on strains and velocities) description of geometrically-nonlinear beams and an unsteady Vortex Lattice aerodynamic model. Construction of a nonlinear, modal-based, reduced order model of the aeroelastic system, employing a state-space realisation of the linearised aerodynamics around an arbitrary reference point, allows us to capture the main nonlinear geometrical couplings at a very low computational cost. Embedding this model in both MHE and MPC strategies, which solve the system continuous-time adjoints efficiently to compute sensitivities, lays the foundations for real-time estimation and control of highly flexible aeroelastic systems. Finally, the performance and versatility of the framework operating in the nonlinear regime is demonstrated on two very flexible wing models, with notably different dynamics, and on two different control setups: a gust-load alleviation problem on a very high aspect ratio wing with slower dynamics, which involves substantial deflections; and flutter suppression on a flexible wing with significantly faster dynamics, where an unconventional nonlinear stabilisation mechanism is unveiled.

Nomenclature

δ_e	=	Control surface deflection
$\boldsymbol{\eta}_a$, $\boldsymbol{\eta}_g$	=	Modal projection of aerodynamic and gravitational forces
$\boldsymbol{\phi}_1$, $\boldsymbol{\phi}_2$, $\boldsymbol{\phi}_\xi$	=	Mode shapes for intrinsic velocities and forces/moments and for quaternions
μ_σ	=	Moment of transfer function at interpolation point
$\boldsymbol{\nu}$	=	Structural nodal coordinates
ρ	=	Free stream density
σ	=	Interpolation point on the complex plane
Σ, Ω, Γ	=	Structural modal-based matrices
τ_s, τ_c, τ_e	=	Sampling period and control/estimation horizons

[*]Graduate research assistant, Room CAGB 308, South Kensington Campus (marc.artola16@imperial.ac.uk)
[†]Graduate research assistant, Room CAGB 308, South Kensington Campus (norberto.goizueta13@imperial.ac.uk)
[‡]Senior Lecturer, Room CAGB 340, South Kensington Campus (a.wynn@imperial.ac.uk)
[§]Professor in Computational Aeroelasticity, Room CAGB 338, South Kensington Campus, Associate Fellow AIAA (r.palacios@imperial.ac.uk)

$\boldsymbol{\xi}$	=	Quaternion defining rotation of the beam elastic axis
ζ	=	Non-dimensional UVLM lattice grid coordinates
$A_\Gamma, B_\Gamma, C_\Gamma, D_\Gamma$	=	Matrices of the continuous-time reduced aerodynamic model
b	=	Wing semi-chord
D_0, D_1, D_2	=	Linear damping matrices
E	=	Initial twist and curvature matrix
$\boldsymbol{f}_\zeta, \boldsymbol{f}_\nu$	=	Non-dimensional aerodynamic forces at UVLM lattice and at structural nodes
k	=	Reduced frequency
L	=	Beam length / wing span
M, C	=	Mass and compliance sectional matrices
N_m	=	Number of structural modes
$\boldsymbol{q_0}$	=	Displacements in modal coordinates
$\boldsymbol{q_1}$	=	Structural velocities in modal coordinates
$\boldsymbol{q_2}$	=	Structural force/moment sectional resultants in modal coordinates
$\boldsymbol{q_\Gamma}$	=	Reduced aerodynamic states
$\boldsymbol{q}_r, \boldsymbol{u}_r$	=	Reference state and control of the control problems
q_∞	=	Dynamic pressure of the free stream
Q_c, Q_e, R_c	=	Control/estimation stage cost weights
$\boldsymbol{r}$	=	Displacements of the beam elastic axis
s	=	Beam spatial coordinate
t	=	Time coordinate
t_∞	=	Free stream time scale
U_∞	=	Free stream velocity
V, Z	=	Model reduction projection matrices
$\boldsymbol{w}$	=	Non-dimensional UVLM external velocities defined at the lattice vertices
w_g	=	Perturbation velocity to free flow due to vertical gust
$\boldsymbol{x}_1, \boldsymbol{x}_2$	=	Intrinsic sectional velocities and forces/moments states

I. Introduction

HIGH-ALTITUDE Platform Stations (HAPS) have captured the interest not only of the major aerospace manufacturers but also of the tech industry, in the pursuit of providing even the most remote areas with internet access. These air-vehicles are the latest demonstration of High-Altitude Long-Endurance (HALE) aircraft which aim to remain airborne almost perpetually. As already mentioned, one of the applications attracting more interest is telecommunications, bringing connectivity to remote areas where conventional terrestrial networks are inaccessible or underdeveloped. Further applications include air-reconnaissance, atmospheric and weather surveillance and other tasks for which satellites

are typically employed, however aiming to perform them at a fraction of the cost.

These structures face notable engineering challenges, mostly due to their light-weight and ultra-slender configurations. Their nominal range of operation is within the stratosphere (around 20 km), where benign meteorological conditions in the form of light winds and low-intensity turbulence prevail and less power is needed to maintain flight [1]. This region is well outside of typical commercial-traffic operational altitudes and also provides the advantage of offering a wide coverage area for telecommunications [2]. It is a key requirement that HAPS vehicles maximise their aerodynamic efficiency to sustain flight solely under solar power. This results in platforms with extremely lightly loaded and very high aspect ratio wings that can benefit from using their increased wing area for solar energy harvesting. However, the slender wings, typically built using lightweight composites, exhibit great flexibility, with deformations comparable to the span, and can pose a severe control challenge. This is especially critical during lower-altitude operations, where they become extremely vulnerable since gusts or turbulence are often encountered and induce large deflections, possibly triggering unstable modes.

Several strategies have been proposed for the aeroelastic control with geometric nonlinearities. The most usual consists of an initial linearisation around an equilibrium/reference point (possibly nonlinear) to then apply standard linear control techniques, such as static output feedback [3] or linear-quadratic-Gaussian (LQG) regulation [4]. Other strategies rely on the manipulation of the underlying nonlinear equations to obtain suitable systems for conventional control methods: for instance, a linear parameter varying system is initially sought in [5], and adaptive control is latter applied, or the case of [6], where proportional-integral-derivative control (PID) or LQG strategies are used after a nonlinear transformation of the original nonlinear system is applied. Model predictive control is experiencing a growing interest for aeroelastic applications for the versatility and ease with which constraints (on states and/or inputs) can be handled [7]. It has widely been used both in gust and manoeuvre load alleviation [8–10] and in trajectory tracking [11] problems. However, linearisation of the discretised state-space representation of aeroelastic systems about a reference steady state or a sequential linearisation about the instantaneous configuration has been the main strategy when applying MPC to date.

In this paper we introduce nonlinear moving horizon estimation (NMHE) and nonlinear model predictive control (NMPC) strategies, which rely on the fully nonlinear simulations deemed essential to capture the main physics of next-generation highly flexible aircraft. In the next lines we summarise the main aspects of the framework, which are aimed at decreasing the computational cost of the implementation, hence paving the way for its application to real-time control of highly flexible aeroelastic systems.

We employ the geometrically nonlinear intrinsic beam equations of [12]. These are a particular formulation of the geometrically exact 1D equations, widely proposed for aeroelastic analysis of slender structures for their agreeable trade-off between model fidelity and computational cost [13, 14]. The intrinsic equations are based on strains and velocities, in contrast to conventional displacement and finite-rotation based formulations. Besides, construction of a

3

modal-based nonlinear low-order model of the intrinsic equations, where few modes are often sufficient to capture the main nonlinear geometrical couplings, has been found to provide an appropriate modelling framework to underpin both the estimator and the predictive controller [15]. To overcome the difficulty of rotations not being directly obtained with the intrinsic equations, they are parametrised using quaternions and approximated by a modal-based expansion, which has also been proven to work satisfactorily embedded in the predictive model [15].

Potential flow theory is widely used to simulate unsteady aerodynamics for aeroelastic analysis, including strip theory [16], unsteady lifting line formulations [17], doublet lattice [18] or unsteady vortex lattice methods (UVLM) [19], in increasing order of computational complexity. The latter approach is chosen, although it often involves systems with thousands of states, since discrete panels (each with one state associated, i.e., circulation) are defined not only to cover each lifting surface but also on their wakes. Employing a linearised version around an arbitrary configuration of the structure we can make use of moment-matching Krylov-subspace techniques to obtain a reduced state-space description of the linear aerodynamics [20]. Of particular interest is to obtain a model in modal coordinates, described in §III.B, which naturally integrates aerodynamic forcing within the low-order nonlinear beam dynamics description. The linearised UVLM formulation assumes small perturbations on the Biot-Savart law, to impose non-penetration boundary conditions on the lifting surface geometry, and a frozen wake geometry. These effects are deemed to be much less relevant than structural nonlinearities, such as the follower force effect of the aerodynamic forcing or the change in the overall dynamics with large deflections, which are successfully captured by means of the geometrically nonlinear beam formulation as shown in §V.

The resulting aeroelastic system is employed as an internal model within our NMHE and NMPC implementations. To improve convergence of the nonlinear problems arising from these estimation and control strategies, a multiple shooting parametrisation of the nonlinear problems (NLPs) [21] is employed. This allows exploiting parallelisation, speeding up the required nonlinear simulations. Further, the implementation of a *real-time iteration* alike scheme [22] can be used to make real-time control of highly flexible aircraft, based on fully nonlinear simulations, attainable for the first time.

A drawback of the multiple shooting parametrisation is that the number of derivatives scales with the square of the system size, hence efficient tools to evaluate them become paramount to make real-time control feasible. In our particular multiple shooting implementation, piecewise continuous-time systems are used to describe the dynamics at each sub-interval. Hence, continuous-time adjoints can be analytically derived, which leverage the quadratic structure of the resulting reduced order model and show more favourable complexity scaling (with respect to the system size) than automatic-differentiation-based sensitivity analysis [15].

The rest of the paper is organised as follows. A brief description of the structural and aerodynamic formulations on which our model is based are given in §II. Subsequently, in §III we show how the structural and aerodynamic low-order models are constructed and merged into a compact aeroelastic description amenable to model-based control and

estimation strategies. Details on the nonlinear estimator and controller implementations are given in §IV. Verification of our implementation and numerical examples on two highly-flexible cantilever wings are provided in §V. The paper concludes with a discussion on future research directions in §VI.

II. Aeroelastic model

A. Structural model

Nonlinear intrinsic beam equations

The dynamics of slender composite beams are described by the intrinsic, geometrically-exact beam theory of Hodges[12]. This formulation uses two vector states, with components in local coordinates, namely the linear and angular inertial velocities vector $x_1(s,t) := [v^\top \; \omega^\top]^\top : [0, L] \times \mathbb{R}_+ \to \mathbb{R}^6$ and the force and moment sectional resultants vector $x_2(s,t) := [f^\top \; m^\top]^\top : [0, L] \times \mathbb{R}_+ \to \mathbb{R}^6$. The curvilinear spatial coordinate is denoted by s, which defines the elastic axis, and t is used to denote time. The arc-length of the undeformed and unloaded structure is denoted by L.

The equations with linear structural damping read

$$M\dot{x}_1 - x_2' - Ex_2 + \mathcal{L}_1(x_1)Mx_1 + \mathcal{L}_2(x_2)Cx_2 = D_0 x_1 + D_1 x_1' + D_2 x_1'' + f_{ext}, \tag{1}$$

$$C\dot{x}_2 - x_1' + E^\top x_1 - \mathcal{L}_1^\top(x_1)Cx_2 = 0, \tag{2}$$

with natural boundary conditions

$$x_{1i}(s_\partial, t) \left(x_2(s_\partial, t) + C_d(s_\partial) \left(x_1'(s_\partial, t) - E^\top x_1(s_\partial, t) \right) \right)_i = 0, \qquad i = 1, \ldots, 6, \; s_\partial \in \{0, L\}, \tag{3}$$

where, for example, x_{1i} denotes the ith entry of the vector x_1. Typically, the boundary conditions are satisfied by enforcing that, in each component, only one of the two factors is zero (i.e., either velocity or force is prescribed for a given degree of freedom at a particular boundary). The matrix C_d is symmetric and positive definite accounting for the damping coefficients in each degree of freedom [23], and

$$D_0 = -(C_d E^\top)' - E C_d E^\top,$$
$$D_1 = C_d' - C_d E^\top + E C_d, \tag{4}$$
$$D_2 = C_d.$$

Matrices $M(s) : \mathbb{R} \to \mathcal{S}_6^{++}$ and $C(s) : \mathbb{R} \to \mathcal{S}_6^+$ are the sectional inertia and compliance matrices, with $\mathcal{S}_6^{++}$ and $\mathcal{S}_6^+$ denoting the set of positive definite and semi-definite symmetric matrices of $\mathbb{R}^{6 \times 6}$, respectively. Matrix $E(s) : \mathbb{R} \to \mathbb{R}^{6 \times 6}$ gathers information on the initial curvature and pre-twist $\kappa_0 \in \mathbb{R}^3$ (i.e., for beams with curvature in an unloaded

5

configuration, such as arched structures),

$$
E = \begin{bmatrix} \widetilde{\kappa}_0 & 0 \\ \widetilde{e}_1 & \widetilde{\kappa}_0 \end{bmatrix},
\tag{5}
$$

where $e_1 = [1\,0\,0]^\top$. Vectors are expressed in a local frame of reference, with origin at the elastic axis and in which all variables and matrices are expressed (see Fig. 1 and Fig. 5). The linear operators $\mathcal{L}_1, \mathcal{L}_2 : \mathbb{R}^6 \to \mathbb{R}^{6\times 6}$ are defined as

$$
\mathcal{L}_1(x_1) = \begin{bmatrix} \widetilde{\omega} & 0 \\ \widetilde{v} & \widetilde{\omega} \end{bmatrix}, \quad \mathcal{L}_2(x_2) = \begin{bmatrix} 0 & \widetilde{f} \\ \widetilde{f} & \widetilde{m} \end{bmatrix}.
\tag{6}
$$

The tilde superscript $\widetilde{a}$ denotes the vector product matrix operator, defined as $\widetilde{a}b = a \times b$, for $a, b \in \mathbb{R}^3$. Prime $(\bullet)'$ and dot $(\dot{\bullet})$ superscripts are used to denote partial derivatives with respect to s and t, respectively. External forces and moments per unit length, acting along the structure (e.g., gravitational, aerodynamic forces), are gathered in the vector f_{ext}.
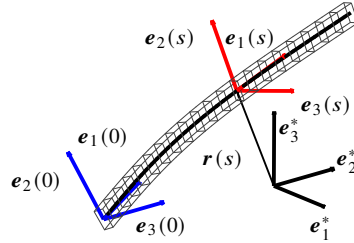

Fig. 1 **Fixed frame of reference e_1^*, e_2^*, e_3^* (black) and local frame of reference e_1, e_2, e_3 at s = 0 (blue) and at an arbitrary location s (red).**

Recovery of displacements and rotations

In the intrinsic formulation, displacements and rotations are secondary variables. Unless the external forcing f_{ext} (e.g., gravity) or some boundary conditions depend on them, they are not required to solve for (1) and (2). A transformation matrix $T(s, t) : [0, L] \times \mathbb{R}_+ \to \mathbb{R}^{3\times 3}$ from the local to the inertial frame (e_1^*, e_2^*, e_3^* in Fig. 1) is defined and quaternions are employed to parametrise finite rotations $\xi(s, t) = [\xi_0, \xi_v^\top]^\top : [0, L] \times \mathbb{R}_+ \to \mathbb{R}^4$, with $\xi_0 \in \mathbb{R}$ and $\xi_v \in \mathbb{R}^3$. They satisfy [24, ch. 26]:

$$
\xi' = \mathcal{U}(\kappa + \kappa_0)\xi,
\tag{7}
$$

$$
\dot{\xi} = \mathcal{U}(\omega)\xi,
\tag{8}
$$

where $\boldsymbol{\kappa}$ is the vector of instantaneous curvatures and twist (i.e., the three last components of the product $C\boldsymbol{x}_2$) and

$$\mathcal{U}(\boldsymbol{a}) = \frac{1}{2}\begin{bmatrix} 0 & -\boldsymbol{a}^\top \\ \boldsymbol{a} & -\widetilde{\boldsymbol{a}} \end{bmatrix}, \qquad \boldsymbol{a} \in \mathbb{R}^3. \tag{9}$$

Given quaternions $\boldsymbol{\xi}$, the corresponding transformation matrix is [24, ch. 6]

$$T(\boldsymbol{\xi}) = (1 - 2\left\|\boldsymbol{\xi}_v\right\|^2)I_3 + 2\boldsymbol{\xi}_v\boldsymbol{\xi}_v^\top + 2\xi_0\widetilde{\boldsymbol{\xi}}_v, \tag{10}$$

where I_3 is the identity matrix in $\mathbb{R}^3$. The displacement field $\boldsymbol{r}$ can be similarly retrieved by solving either of the equations

$$\boldsymbol{r}' = T(\boldsymbol{e}_1 + \boldsymbol{\gamma}), \tag{11}$$

$$\dot{\boldsymbol{r}} = T\boldsymbol{v}, \tag{12}$$

where $\boldsymbol{\gamma}$ is the strain vector (i.e., the three first components of $C\boldsymbol{x}_2$).

Taking gravity as an example of an orientation-dependent forcing term, the evolution equation for the quaternions (8) would need to be added to equations (1) and (2), and its contribution in the momentum balance equation (1) would read

$$\boldsymbol{f}_g(s, t) = \mu(s)\begin{bmatrix} I_3 \\ \widetilde{\boldsymbol{r}}_{cm}(s) \end{bmatrix}T(s, t)^\top \boldsymbol{g}, \tag{13}$$

where $\boldsymbol{r}_{cm}$ is the offset distance between the sectional centre of mass and the elastic axis ($\boldsymbol{r}_{cm}$ is a fixed parameter and depends on the beam's cross sectional properties), which produces a torque about the latter. The vector $\boldsymbol{g}$ is the gravity acceleration, which is expressed in the global frame of reference.

B. Aerodynamic model

The chosen aerodynamic model consists of an unsteady vortex lattice method (UVLM) formulation. This model has been implemented in the aeroelastic simulation tool SHARPy [25], developed in-house and available as open-source. It is described in detail in [19, 26, 27] and we therefore keep this section brief to explain only the details of the linearised description and the coupling process with the structural model.

The UVLM is a medium fidelity, potential-flow method in which the lifting surfaces and wakes are discretised into a lattice of vortex rings. These vortices induce a velocity in the flow field according to the Biot-Savart law and the vortex strength is resolved by enforcing the non-permeability boundary conditions at the bound panels' collocation points. The boundary conditions that enforce the non-permeability condition introduce the time dependency into the problem

since they are functions of the instantaneous lifting surface geometry and kinematics. Similarly, the wake consists of a discrete lattice of free vortex panels whose circulation is determined by the convection of the shed bound panels at the trailing edge and its shape is affected not only by this shed circulation but also by the wake itself, therefore being capable of capturing wake roll-up effects. Aerodynamic forces are then resolved at the lattice vertices, where the steady contribution is calculated using the Joukowsky method [28, 29] and the unsteady forces using Bernoulli's equation, dependent on the time derivative of the circulation.

The formulation is nonlinear due to the dependency of the aerodynamic influence coefficients on the instantaneous shape, requiring that they be updated at every iteration. However, the model can be linearised around a reference condition and assuming a frozen wake geometry [20]. Finally, a non-dimensional implementation is considered for the aerodynamic model to be valid across all (incompressible) flight speeds provided that the vehicle's shape does not change significantly. Therefore the perturbation variables around the linearisation point $\delta(\bullet)$ are scaled by the reference dimensions: flight velocity, U_∞, the semi-chord for length dimensions, b, and the free stream density, ρ. Consequently, the UVLM expressed in normalised time, $\hat{t} = U_\infty t / b$, results in a discrete, linear time-invariant, state-space formulation of the form

$$
\begin{aligned}
\boldsymbol{x}^{n+1} &= A_{\text{aero}} \boldsymbol{x}^n + B_{\text{aero}} \boldsymbol{u}^{n+1}, \\
\boldsymbol{y}^n &= C_{\text{aero}} \boldsymbol{x}^n + D_{\text{aero}} \boldsymbol{u}^n,
\end{aligned}
\tag{14}
$$

where the state is the vector of non-dimensional bound and wake $(\bullet)_w$ panel circulations, circulation derivatives and previous bound circulations $\boldsymbol{x}^n = [\delta \boldsymbol{\Gamma}^n, \delta \boldsymbol{\Gamma}_w^n, \Delta \hat{t} \delta \dot{\hat{\boldsymbol{\Gamma}}}^n, \delta \boldsymbol{\Gamma}^{n-1}] \in \mathbb{R}^{3K+K^*}$, where $(\dot{\hat{\bullet}})$ is used to denote derivatives with respect to the normalised time, and K and K^* are the number of bound and wake panels, respectively. The input to the system is defined by $\boldsymbol{u}^{n+1} = [\delta \boldsymbol{\zeta}^{n+1}, \delta \dot{\hat{\boldsymbol{\zeta}}}^{n+1}, \delta \boldsymbol{w}^{n+1}] \in \mathbb{R}^{9K_\zeta}$, where $\boldsymbol{\zeta}$ and $\dot{\hat{\boldsymbol{\zeta}}}$ correspond to the non-dimensional grid coordinates and velocities, $\boldsymbol{w}$ to non-dimensional external velocities and K_ζ is the number of grid vertices. The output is simply the non-dimensional forces at those vertices $\boldsymbol{y}^n = \delta \boldsymbol{f}_\zeta^n \in \mathbb{R}^{3K_\zeta}$. Note that the input to the system is atypically defined at time step $n + 1$. This is due to the elliptical nature of the underlying partial differential equations (PDEs) such that disturbances are felt instantaneously everywhere across the flow field.

III. Low-order nonlinear aeroservoelastic model

A. Modal-based structural low-order model

The structural low-order model is built from its Linear Normal Modes (LNMs) [30]. Also referred to as mode shapes, they are the eigenfunctions $\boldsymbol{\phi}_{1j}(s), \boldsymbol{\phi}_{2j}(s) : [0, L] \to \mathbb{R}^6$ of the linearised differential equations (1) and (2) around the origin, with no external forcing (i.e., $\boldsymbol{f}_{ext} = \boldsymbol{0}$) and no damping ($D_i = 0$). Using N_m eigenfunctions, an

approximation to the state variables is constructed:

$$x_1(s, t) = \boldsymbol{\phi}_{1j}(s) q_{1j}(t), \tag{15}$$

$$x_2(s, t) = \boldsymbol{\phi}_{2j}(s) q_{2j}(t), \tag{16}$$

where $q_{1j}(t)$, $q_{21j}(t) : \mathbb{R}_+ \to \mathbb{R}$ are the temporal coefficients of the expansion (unless otherwise stated, Einstein's summation convention for index $j = 1, ..., N_m$ is used). The low-order model is then obtained by a Galerkin projection, in which evolution equations for the expansion weights q_{1j} and q_{2j} are obtained by substituting (15) and (16) into (1) and (2), pre-multiplying each set of equations by the eigenfunctions and integrating over the spatial domain.

The resulting reduced order model has the form

$$\dot{\boldsymbol{q}} = W\boldsymbol{q} + N(\boldsymbol{q})\boldsymbol{q} + \begin{bmatrix} \boldsymbol{\eta} \\ \mathbf{0} \end{bmatrix}, \tag{17}$$

where the expansion temporal coefficients are gathered in a column vector $\boldsymbol{q}(t) = [\boldsymbol{q}_1^\top \; \boldsymbol{q}_2^\top]^\top : \mathbb{R}_+ \to \mathbb{R}^{2N_m}$. The modes around the unloaded configuration are orthogonal [31], and, if normalised so that $\langle \boldsymbol{\phi}_{1i}, M\boldsymbol{\phi}_{1j} \rangle = \langle \boldsymbol{\phi}_{2i}, C\boldsymbol{\phi}_{2j} \rangle = \delta_{ij}$, where δ_{ij} is the Kronecker delta, the matrix W has the form

$$W = \begin{bmatrix} \Sigma & \Omega \\ -\Omega & 0 \end{bmatrix}, \tag{18}$$

where Ω is a diagonal matrix whose entries are the eigenvalues of the linearised system and Σ is the damping matrix in modal coordinates

$$[\Sigma]_{ij} = \left\langle \boldsymbol{\phi}_{1i}, D_0\boldsymbol{\phi}_{1j} + D_1\boldsymbol{\phi}'_{1j} + D_2\boldsymbol{\phi}''_{1j} \right\rangle. \tag{19}$$

The term $N(\boldsymbol{q})$ is skew-symmetric and linear in $\boldsymbol{q}$,

$$N(\boldsymbol{q}) = \begin{bmatrix} -q_{1l}\Gamma_1^l & -q_{2l}\Gamma_2^l \\ q_{2l}(\Gamma_2^l)^\top & 0 \end{bmatrix}, \tag{20}$$

with constant matrices

$$\left[\Gamma_1^l\right]_{ij} = \left\langle \boldsymbol{\phi}_{1i}, \mathcal{L}_1(\phi_{1j}) M \boldsymbol{\phi}_{1l} \right\rangle, \tag{21}$$

$$\left[\Gamma_2^l\right]_{ij} = \left\langle \boldsymbol{\phi}_{1i}, \mathcal{L}_2(\phi_{2j}) C \boldsymbol{\phi}_{2l} \right\rangle. \tag{22}$$

9

The entries of the forcing term vector are

$$[\boldsymbol{\eta}]_i = \langle \boldsymbol{\phi}_{1i}, \boldsymbol{f}_{ext} \rangle, \tag{23}$$

which in our case will gather contributions from gravity and aerodynamic forces. Further details on the derivation of this low-order model and its properties are contained in [32]. The instantaneous energy of the system (kinetic + elastic potential) written in modal coordinates is, simply,

$$\epsilon(t) = \frac{1}{2} \boldsymbol{q}^\top \boldsymbol{q}, \tag{24}$$

with ϵ satisfying $\dot{\epsilon} = \boldsymbol{q}_1^\top \boldsymbol{\eta} + \boldsymbol{q}_1^\top \Sigma \boldsymbol{q}_1$.

Displacements and rotations

The following expansion for the quaternions is defined

$$\boldsymbol{\xi}(s,t) = \boldsymbol{\phi}_{\xi j}(s) q_{\xi j}(t), \ \ j = 0, 1, \cdots, N_m, \tag{25}$$

where $\boldsymbol{\phi}_{\xi 0} = \bar{\boldsymbol{\xi}}$ is employed as a *shifting equilibrium* mode [15], with $\bar{\boldsymbol{\xi}}$ defining the undeformed rotation field given by $\bar{\boldsymbol{\xi}}' = \mathcal{U}(\kappa_0)\bar{\boldsymbol{\xi}}$. We now define the remaining mode shapes, $\phi_{\xi j}, \ j = 1, \cdots, N_m$, to be the eigenfunctions of the linearised equation (8) around the unloaded and undeformed condition,

$$\Delta \dot{\boldsymbol{\xi}} = \mathcal{U}_\omega(\bar{\boldsymbol{\xi}}) \Delta \omega, \tag{26}$$

where

$$\mathcal{U}_\omega(\bar{\boldsymbol{\xi}}) = \frac{\partial}{\partial \omega} \left(\mathcal{U}(\omega)\bar{\boldsymbol{\xi}} \right) = \begin{bmatrix} -\bar{\boldsymbol{\xi}}_v^\top \\ \bar{\xi}_0 I_3 + \widetilde{\bar{\boldsymbol{\xi}}}_v \end{bmatrix}. \tag{27}$$

Finally, mode shapes for the quaternions are obtained from (26) using the velocity modes $\boldsymbol{\phi}_{1j}$

$$\boldsymbol{\phi}_{\xi j} = \mathcal{U}_\omega(\bar{\boldsymbol{\xi}}) \boldsymbol{\phi}_{\omega j}, \tag{28}$$

where $\boldsymbol{\phi}_{\omega j} = \Pi_\omega \boldsymbol{\phi}_{1j}$, and $\Pi_\omega = [0_3, I_3]$ is a truncation operator used to retrieve the angular velocity components.

The evolution equation for $\boldsymbol{q}_\xi$, obtained by Galerkin projection of (8), and the gravity forcing term $\boldsymbol{\eta}_g$, obtained using equations (10) and (13) read

$$A_\xi \dot{\boldsymbol{q}}_\xi = N_\xi(\boldsymbol{q}_\xi) \boldsymbol{q}_1, \tag{29}$$

and

$$\boldsymbol{\eta}_g = \boldsymbol{\eta}_{g_0} + \eta_g(\boldsymbol{q}_\xi). \tag{30}$$

The matrices $N_\xi(\boldsymbol{q}_\xi) = q_{\xi l}\Gamma_\xi^l$ and $\eta_g(\boldsymbol{q}_\xi) = q_{\xi l}\Gamma_g^l$ depend linearly on $\boldsymbol{q}_\xi$, with constant coefficients

$$\left[\Gamma_\xi^l\right]_{ij} = \left\langle \boldsymbol{\phi}_{\xi i}, \mathcal{U}(\boldsymbol{\phi}_{\omega j})\boldsymbol{\phi}_{\xi l} \right\rangle, \tag{31}$$

$$\left[\Gamma_g^l\right]_{ij} = \left\langle \boldsymbol{\phi}_{1i}, \mu \begin{bmatrix} I_3 \\ \widetilde{\boldsymbol{r}}_{cm} \end{bmatrix} T_\phi(\boldsymbol{\phi}_{\xi j}, \boldsymbol{\phi}_{\xi l})^\top \boldsymbol{g} \right\rangle, \tag{32}$$

where

$$T_\phi(\boldsymbol{\xi}^{(a)}, \boldsymbol{\xi}^{(b)}) = -2\boldsymbol{\xi}_v^{(a)\top}\boldsymbol{\xi}_v^{(b)}I_3 + 2\boldsymbol{\xi}_v^{(a)}\boldsymbol{\xi}_v^{(b)\top} + 2\xi_0^{(a)}\widetilde{\boldsymbol{\xi}_v^{(b)}}, \tag{33}$$

and A_ξ is a constant matrix

$$[A_\xi]_{ij} = \left\langle \boldsymbol{\phi}_{\xi i}, \boldsymbol{\phi}_{\xi j} \right\rangle. \tag{34}$$

Here, $\langle \cdot, \cdot \rangle$ denotes the L^2-inner product in $L^2([0, L])^4$ and $L^2([0, L])^6$ indistinctly. The constant term in (30) is obtained by setting $T_\phi = I_3$ in (32).

Since displacements are not required to time-march the resulting structural low-order model, no reduction technique to decrease the computational cost to evaluate them is sought. Hence, at a given spatial coordinate s, they can be obtained by mere post-processing of the modal solution via the temporal evolution equation

$$\dot{\boldsymbol{r}}(s) = T(\phi_{\xi i}(s)q_{\xi i})\boldsymbol{\phi}_{vj}(s)q_{1j}, \tag{35}$$

obtained by inserting the modal expansions (15) and (25) into (12), and where $\boldsymbol{\phi}_{vj} = \Pi_v\boldsymbol{\phi}_{1j}$, with $\Pi_v = [I_3, 0_3]$ the truncation operator used to retrieve the translational velocity components.

B. Linear UVLM ROM using Moment Matching

The aerodynamic model described by the UVLM is usually large in size given the requirements of a very fine discretisation of the bound panels to achieve convergence to an adequate accuracy [20, 33]. In addition, the convection of the bound panels onto the wake results in a very refined wake, which is normally large (order of 10-100 chords). Usual systems that compare well to benchmark results have dimensions of the order $O(10^4 - 10^5)$ and are unsuitable for control synthesis. Therefore, we must turn to model reduction techniques.

Model reduction by moment matching is a very attractive model order reduction technique for this application since it is based on the use of Krylov subspaces, which are highly efficient when dealing with large sparse systems [34]. Plus,

the technique offers the flexibility of defining interpolation points at which the transfer function is approximated. This fits well with the physical characteristics of the aeroelastic systems, where the relevant dynamics are typically well below reduced frequencies of $k < 1$ [35]. Furthermore, the linearised UVLM formulation lacks saturation to added mass and damping effects and therefore, as the the frequency approaches the Nyquist limit $k_N = \pi/\Delta\hat{t}$, their magnitude continues to grow quadratically [20]. Therefore, the interest will reside in interpolating the transfer function at low frequencies only. However, to achieve an efficient reduction the number of inputs and outputs must be reduced to lower the number of transfer functions to interpolate, given that the method is based on transfer function interpolation.

Since the inputs and outputs of the linearised UVLM system in (14) are defined at the lattice vertices, the number of transfer functions will inevitably be large whenever a refined grid discretisation is employed. Thus, the dimension of the inputs and outputs must be first reduced in order for the Krylov reduction to be effective. Under the assumptions that the wing's cross section rotates rigidly and that the structural nodes coincide in their spanwise location with the edges of the UVLM panels, the UVLM inputs (the dimensional grid displacements $b\zeta$ and velocities $U_\infty\dot{\hat{\zeta}}$) and outputs (non-dimensional forces at the lattice vertices, f_ζ) can be projected onto the structural nodal coordinates, ν, using the linear mappings defined by the constant matrices K:

$$b\zeta = K_\nu\nu, \qquad U_\infty\dot{\hat{\zeta}} = K_\nu\dot{\nu}, \text{ and } f_\nu = K_F f_\zeta.$$

These mappings are based on the coincident spanwise discretisation of the UVLM lattice and the underlying structural beam, which simplifies them and requires no use of interpolation. Of the two systems, it is the UVLM the one that requires a finer discretisation, however, since eventually it will be projected onto modal coordinates there is no penalty arising from the structural system being too finely discretised. For time domain simulations where the UVLM discretisation poses too much of a penalty on the simulation, a scheme with differing structural and aerodynamic time steps has been devised, while keeping the strong coupling between the two [36].

With the UVLM expressed in the structural nodal coordinates, the number of inputs and outputs is reduced considerably, yet it can be reduced even further by projecting the inputs and outputs onto the modal space using mode functions derived in the previous section for the benefit of the Krylov reduction method. The resulting discrete-time, state-space representation of the modal projection of the UVLM is shown in Fig. 2, where q_0 and $bU_\infty^{-1}q_1$ are the (time-scaled, recall the dimensionless definition of the UVLM in Section II.B) intrinsic displacement and velocities modal coordinates, which expand the structural nodal coordinates: $\nu = \phi_{1j}q_{0j}$, $\dot{\nu} = \phi_{1j}q_{1j}$. The system's output consists then of modal aerodynamic forces, η_a (i.e., the projection onto the modal space of the aerodynamic force f_ν), which are non-dimensional and shall be scaled with the reference dynamic pressure and semi-chord $q_\infty b^2$, with $q_\infty = \frac{1}{2}\rho U_\infty^2$. As for the remaining inputs, a single control surface is implemented with deflection angle δ_e and rate $\dot{\delta}_e$ (mapped onto the lattice grid coordinates and velocities). Additionally, a gust system, G_{gust}, is introduced to convect
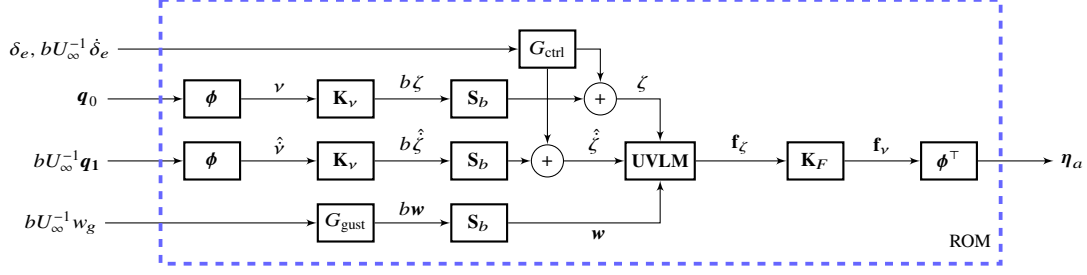
Fig. 2 Block diagram description of the reduced aerodynamic system projected onto modal coordinates with gust and control surface inputs.

downstream and map uniformly across the span an external vertical velocity defined at the leading edge, reducing $w \in \mathbb{R}^{3K_\zeta}$ to a single input, w_g (note that the extension to multiple control surface inputs or external velocities is straightforward).

We now make use of moment matching to reduce the system outlined in Fig. 2. The transfer function of a generic, linear, multi-input multi-output, time-invariant system can be described in terms of the complex variable, $s \in \mathbb{C}$ as $H(s) = C(sI - A)^{-1}B$ (for the purposes of model reduction and to keep the notation concise, $D = 0$ will be assumed without any loss of generality and the notation for a continuous-time system will be employed, being the method completely applicable to the discrete-time case). Such a transfer function can be represented by a power series expansion in the vicinity of an arbitrary point in the complex plane $\sigma \in \mathbb{C}$ as

$$H(s) = \sum_{j=0}^{\infty} \mu_\sigma^j (\sigma - s)^j, \tag{36}$$

where the coefficients μ_σ^j define the j-th moment of the system at σ. These are related to the transfer function derivatives by

$$\mu_\sigma^j = \frac{(-1)^j}{j!} \frac{d^j}{ds^j} H(s) \bigg|_{s=\sigma} \tag{37}$$

which are equal to

$$\mu_\sigma^j = C(\sigma I - A)^{-(j+1)} B, \ j \geq 0. \tag{38}$$

A reduced order model by moment matching is built by matching the first r moments of the original transfer function expansion at σ, namely

$$\mu_\sigma^j = \hat{\mu}_\sigma^j \text{ for } j \in \{1, \ldots, r\}, \text{where } r < n, \tag{39}$$

where r and n are the reduced and full order state vector dimensions and $\hat{\mu}_\sigma^j$ is the j-th moment of the reduced order model evaluated at $\sigma \in \mathbb{C}$.

Although the moments have been defined in (37), they are never computed explicitly since the subsequent derivatives

13

involve matrix powers that would lead to ill-conditioned and unstable numerical procedures [37, ch. 11]. However, one can turn to projection methods and Krylov subspaces to obtain a reduced order model by moment matching without directly computing them.

The definition of an *i*-th order Krylov subspace is $\mathcal{K}_i(F, \mathbf{g}) := \text{span}(\mathbf{g}, F\mathbf{g}, F^2\mathbf{g}, \ldots, F^{i-1}\mathbf{g})$ with $F \in \mathbb{R}^{n \times n}$ and $\mathbf{g} \in \mathbb{R}^n$. Therefore, given the expression in (38), one can build certain Krylov subspaces that contain information of the moments. At interpolation points $\sigma \in \mathbb{C}$, the corresponding Krylov subspaces that guarantee that the reduced system matches the moments of the full order system at that point are

$$
\mathcal{K}_{r_b}\left((\sigma I - A)^{-1}, (\sigma I - A)^{-1}B\right) \subseteq \mathcal{V} = \text{span}(V),
$$
$$
\mathcal{K}_{r_c}\left(\left((\sigma I - A)^{-1}\right)^\top, \left((\sigma I - A)^{-1}\right)^\top C^\top\right) \subseteq \mathcal{Z} = \text{span}(Z),
$$
(40)

where V and Z are the projection matrices that span the relevant Krylov subspaces and are used to reduce the full order system.

The only requirement applicable to the interpolation point $\sigma \in \mathbb{C}$ is that it is not an eigenvalue of A. The case of matching the moments at infinity is referred to as partial realisation and in that case the Krylov subspaces are built simply using $\mathcal{K}_{r_b} = (A, B)$. In addition, the method is not restricted to a single interpolation point and many can be used, in which case the projection matrices would simply span the union of the different Krylov subspaces that are constructed for each of them.

The use of the Krylov subspaces is well suited for very large systems since the matrices that span the subspaces, V and Z, can be built using the Arnoldi iteration that is typically used to calculate the eigenvalues of high-dimensional matrices [38]. However, the rational interpolation case about finite frequencies does introduce an overhead to compute a LU factorisation of the $(\sigma I - A)$ matrices of (40) (albeit this only needs to be done once for each interpolation point and is then stored in memory). Hence, the remainder of the iteration is based on efficient matrix-vector multiplications [39].

Lastly, the expansion to the multi-input multi-output (*m* inputs, *p* outputs) space can be approached in two ways: the tangential interpolation methods of Gallivan [40] or the blockwise construction method of the Krylov space of Gugercin [39]. The former is based on the use of 'tangential direction' vectors that effectively interpolate certain transfer functions attending to some *a priori* knowledge of which ones are the ones that have the greatest effect on the system. Gugercin's method, on the other hand, is based on the construction of the projection matrices one block at a time, one for each input or output, and removing those that create a linear dependency in the projection matrices. This is the method of choice for the current application given its generality and lack of heuristics. Note however, that in either case the size of the ROM is highly dependent upon the number of inputs and outputs and therefore one must strive to achieve a formulation that reduces them as much as possible. In the case at hand, the projection of the UVLM onto the structural modal space makes for an effective input/output reduction method, reducing the original problem with

$O(10^2 - 10^3)$ inputs to just a few modes.

The projection matrices that span the Krylov subspaces are constructed using an Arnoldi iteration with a modified Gram-Schmidt orthogonalisation. This is performed in a vector-wise manner (i.e., each input or output vector in B or C) as shown in Algorithm 1, which can be used in an analogous manner to obtain Z.

Algorithm 1 Constructing V using the Arnoldi iteration with Modified Gram-Schmidt orthogonalisation

---

1: $m \leftarrow 0$ {counter}
2: $V \leftarrow [\,]$
3: **for** $j = 1 : r_b$ **do**
4:     **if** j = 1 **then**
5:         $\tilde{v}_m \leftarrow (\sigma I - A)^{-1} B$
6:     **else**
7:         $\tilde{v}_m \leftarrow (\sigma I - A)^{-1} v_{m-1}$ {v_{m-1} is the $(m-1)$-th column vector of V}
8:     **end if**
9:     $\hat{v}_m \leftarrow \tilde{v}_m - VV^T \tilde{v}_m$
10:    $V \leftarrow [V, \tilde{v}_m / ||\hat{v}_m||]$
11:    $m \leftarrow m + 1$
12: **end for**

This method described for any linear time-invariant system can now be applied on the full-order discrete-time UVLM system (14), where the reduced aerodynamic state vector, with dimension $k = N_\Gamma = 2N_m N_\sigma r_b$ (i.e., twice the number of modes – the inputs are modal displacements and velocities –, times the number of interpolation points times the number of moments matched at each interpolation point) is now approximated by $\boldsymbol{q}_\Gamma \approx V\boldsymbol{x} \in \mathbb{R}^{N_\Gamma}$. Since the matrices V and Z satisfy $Z^\top V = I$, the reduced aerodynamic system is assembled as:

$$\left(\begin{array}{c|c} \hat{A} & \hat{B} \\ \hline \hat{C} & \hat{D} \end{array} \right) \text{with} \begin{cases} \hat{A} = Z^\top A_{\text{aero}} V \in \mathbb{R}^{k \times k} \\ \hat{B} = Z^\top B_{\text{aero}} \in \mathbb{R}^{k \times m} \\ \hat{C} = C_{\text{aero}} V \in \mathbb{R}^{p \times k} \\ \hat{D} = D_{\text{aero}} \in \mathbb{R}^{p \times m} \end{cases} . \tag{41}$$

The reduced order model is thus built using the projector matrices which span an orthonormal basis and satisfy the moment matching condition [37, ch. 11].

Finally, to permit the coupling with the structural model defined in continuous time, a bilinear transformation [37] is applied to the discrete-time system given by (41) applying the corresponding matrix transformations [41] to $(\hat{A}, \hat{B}, \hat{C}, \hat{D})$ to obtain an approximation to its continuous-time counterpart $(A_\Gamma, B_\Gamma, C_\Gamma, D_\Gamma)$. The resulting linear continuous-time state-space realisation of UVLM expressed in the structure's modal space, accounting for the corresponding relationship between dimensional and non-dimensional time $t = bU_\infty^{-1}\hat{t}$, takes the form of

$$bU_\infty^{-1}\dot{\boldsymbol{q}}_\Gamma = A_\Gamma \boldsymbol{q}_\Gamma + B_{q_0}\boldsymbol{q}_0 + bU_\infty^{-1}B_{q_1}\boldsymbol{q}_1 + bU_\infty^{-1}B_w w_g + B_\delta \delta_e + bU_\infty^{-1}B_{\dot{\delta}}\dot{\delta}_e, \tag{42}$$
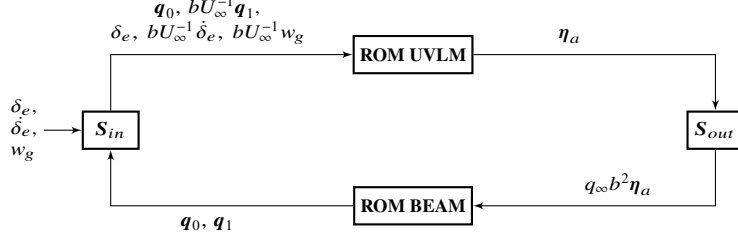
Fig. 3   Coupled aeroelastic system with reduced aerodynamics and structural modules.

$$\boldsymbol{\eta}_a = \bar{\boldsymbol{\eta}}_a + C_\Gamma \boldsymbol{q}_\Gamma + D_{q_0}\boldsymbol{q}_0 + bU_\infty^{-1}D_{q_1}\boldsymbol{q}_1 + bU_\infty^{-1}D_w w_g + D_\delta \delta_e + bU_\infty^{-1}D_{\dot\delta}\dot\delta_e, \tag{43}$$

where $\bar{\boldsymbol{\eta}}_a$ denotes the possible non-zero aerodynamic force at the arbitrary configuration at which the UVLM is linearised and input matrices have been split into the diverse contributions of modal displacements ($\boldsymbol{q}_0$), velocities ($\boldsymbol{q}_1$), the external vertical gust velocity (w_g) and control surface deflections and velocities ($\delta, \dot\delta$), such that $B_\Gamma = [B_{q_0}, B_{q_1}, B_w, B_\delta, B_{\dot\delta}]$ and $D_\Gamma = [D_{q_0}, D_{q_1}, D_w, D_\delta, D_{\dot\delta}]$. Note that, for simplicity, the terms arising from the perturbation on dynamic pressure have not been included but they can be incorporated with ease for systems, such as free-flying aircraft, that require them.

C. Aeroelastic integration

Hitherto, the chosen structural and aerodynamic models alongside their appropriate model reduction methods have been described and only the coupling between them to yield the full aeroelastic formulation remains. The structural system has been expressed in modal coordinates and the UVLM inputs/outputs employs such mode shapes to project the inputs/outputs onto the same modal space.

The complete nonlinear aeroelastic system consists of the structural equations (17), together with the quaternion's evolution equation (29) and the aerodynamic reduced order model (42). With these two last equations, gravity (30) and aerodynamic forcing contributions (43) can be readily evaluated. An extra equation accounting for the displacement modal coefficients, $\boldsymbol{q}_0$, obtained from direct integration of the velocity modal coordinates, $\boldsymbol{q}_1$, is included as required by the aerodynamic model. Written in modal coordinates, the system reads

$$\dot{\boldsymbol{q}}_0 = \boldsymbol{q}_1,$$

$$\dot{\boldsymbol{q}}_1 = \Sigma\boldsymbol{q}_1 + \Omega\boldsymbol{q}_2 - q_{1l}\Gamma_1^l\boldsymbol{q}_1 - q_{2l}\Gamma_2^l\boldsymbol{q}_2 + \boldsymbol{\eta}_{g_0} + q_{\xi l}\Gamma_g^l\boldsymbol{q}_\xi$$

$$+ q_\infty b^2\big(\bar{\boldsymbol{\eta}}_a + C_\Gamma\boldsymbol{q}_\Gamma + D_{q_0}\boldsymbol{q}_0 + t_\infty D_{q_1}\boldsymbol{q}_1 + t_\infty D_w w_g + D_\delta\delta_e + t_\infty D_{\dot\delta}\dot\delta_e\big),$$

$$\dot{\boldsymbol{q}}_2 = -\Omega\boldsymbol{q}_1 + q_{2l}(\Gamma_2^l)^\top\boldsymbol{q}_1, \tag{44}$$

$$\dot{\boldsymbol{q}}_\xi = q_{\xi l}A_\xi^{-1}\Gamma_\xi^l\boldsymbol{q}_1,$$

$$\dot{\boldsymbol{q}}_\Gamma = t_\infty^{-1}\big(A_\Gamma\boldsymbol{q}_\Gamma + B_{q_0}\boldsymbol{q}_0 + t_\infty B_{q_1}\boldsymbol{q}_1 + t_\infty B_w w_g + B_\delta\delta_e + t_\infty B_{\dot\delta}\dot\delta_e\big),$$

16

where matrices Σ, Ω and Γ are as in §III.A, and $q_\infty = \frac{1}{2}\rho U_\infty^2$ and $t_\infty = bU_\infty^{-1}$ are the dynamic pressure and convective time scale of the free stream. These are the scaling factors, S_{in} and S_{out}, between the structural and aerodynamic modules [20] shown in the coupled system block diagram in Fig. 3. The control surface's kinematics can be described solely by one of its inputs, in this case, the rate of deflection is chosen as the control input $u(t)$ (no actuator model is considered here) leaving the deflection angle as a new state $q_\delta = \delta_e$, subject to the time evolution equation

$$\dot{q}_\delta = \dot{\delta} = u(t). \tag{45}$$

The vertical gust velocity is chosen as the disturbance $w(t) = w_g$ to our system, notation which will be followed throughout the following sections. The dimensionality of the resulting system (44)–(45) is of the order of $O(50)$, since usually the first 5–10 structural modes contain enough information for typical control problems (e.g. flutter suppression, gust-load alleviation or manoeuvring problems) and the aerodynamic states can be reduced to $10 - 20$ states without significantly compromising the accuracy of the reduced-order description.

IV. Nonlinear estimator and controller

The coupled aeroelastic system (44)–(45) is very suitable as an internal model for control since it efficiently captures geometrical nonlinear effects present in very flexible aeroelastic systems, condensed in a considerably small state space vector. To describe the implementation of the nonlinear estimation and model predictive control strategies the aeroelastic modal reduced order model, as defined in (44), is used, however extending it straightforwardly to multiple inputs and disturbances.

Nonlinear model predictive control aims to provide control feedback by solving repetitively at each sampling point t_i, with a sampling period τ_s, the following nonlinear optimal control problem over a time horizon τ_c:

$$\begin{aligned}
\min_{u(t)} \quad & \int_{t_i}^{t_i+\tau_c} V_c(q_{ae}, u(t))\, dt \\
\text{s.t.} \quad & h(\dot{q}_{ae}, q_{ae}, u(t), w(t)) = 0, \\
& q_{ae}(t_i) = q_{ae}^c, \\
& q_{ae_{min}} \le q_{ae} \le q_{ae_{max}}, \\
& u_{min} \le u(t) \le u_{max},
\end{aligned} \tag{46}$$

where $q_{ae} = [q_0^\top \, q_1^\top \, q_2^\top \, q_\xi^\top \, q_\Gamma^\top \, q_\delta^\top]^\top$ is the augmented, modal aeroelastic states vector, $u(t)$ defines the system control inputs and $w(t)$ gathers the influence of external disturbances to the system. Box constraints on the control input and possibly on some of the states are considered (e.g., aileron deflection angle constraints). The functional $V_c(q_{ae}, u(t))$ is

17

a cost function chosen to have a quadratic form as

$$V_c = \frac{1}{2} \left(\boldsymbol{q}_{ae} - \boldsymbol{q}_r\right)^\top Q_c \left(\boldsymbol{q}_{ae} - \boldsymbol{q}_r\right) + \frac{1}{2} \left(\boldsymbol{u} - \boldsymbol{u}_r\right)^\top R_c \left(\boldsymbol{u} - \boldsymbol{u}_r\right),$$

(47)

for some weighting matrices $Q_c \geq 0$ and $R_c \geq 0$, reference state $\boldsymbol{q}_r$ and control $\boldsymbol{u}_r$. The functional $\boldsymbol{h}$ represents the set of ODEs (44)–(45) and $\boldsymbol{q}_{ae}^c$ is the sample obtained from the actual system at $t = t_i$, initial condition of the MPC problem. This sample, in turn, can be obtained by solving a further nonlinear program, given by a (nonlinear) moving horizon estimation problem cast in the following form

$$\min_{w(t),\,\boldsymbol{q}_{ae}^e} \int_{t_i-\tau_e}^{t_i} V_e(\boldsymbol{y},\boldsymbol{y}_e)\,dt$$

$$\text{s.t.} \quad \boldsymbol{h}(\dot{\boldsymbol{q}}_{ae},\boldsymbol{q}_{ae},\boldsymbol{u}(t),\boldsymbol{w}(t)) = 0,$$

$$\boldsymbol{q}_{ae}(t_i - \tau_e) = \boldsymbol{q}_{ae}^e,$$

$$\boldsymbol{q}_{ae}(t_i) = \boldsymbol{q}_{ae}^c.$$

(48)

Here, the unknown parameters found upon solution of the above nonlinear problem are the external disturbances $\boldsymbol{w}(t)$ together with the initial state of the system $\boldsymbol{q}_{ae}^e$ at the beginning of the estimation horizon τ_e. The functional $\boldsymbol{h}$ in (48) is the same system as in (46), and terminal constraints on some of the states are considered (e.g., aileron deflection angle is known at the sampling time). Now, the functional subject to minimisation V_e aims at penalising the error between a measured output $\boldsymbol{y}$ from the actual system and the estimated output produced by the internal model, which is chosen to be a linear function of the vector state, $\boldsymbol{y}_e = \mathcal{L}(\boldsymbol{q}_{ae})$. Similarly, a quadratic functional is used to construct V_e using a weighting matrix $Q_e \geq 0$,

$$V_e = \frac{1}{2} \left(\boldsymbol{y} - \boldsymbol{y}_e\right)^\top Q_e \left(\boldsymbol{y} - \boldsymbol{y}_e\right).$$

(49)

Once the NLP (48) is solved, the final state of the estimation window $\boldsymbol{q}_{ae}$ at $t = t_i$, corresponds to the estimated initial condition $\boldsymbol{q}_{ae}^c$ of the MPC problem (46).

The nonlinear problems arising from the estimation and control strategies are very similar and can be solved in almost identical procedures. Hence, the NMPC problem is taken as an example for the implementation description that follows along the next lines.

A. NLP solution strategy

Application of multiple shooting parametrisation [21] to the problem yields a split of the prediction horizon τ_c into M_c time subintervals (with superscript $m = 1, \cdots, M_c$ denoting that the variable belongs to the mth interval with $t_{m-1} \leq t \leq t_m$) and the addition of each of the subintervals' initial conditions to the optimisation parameters. Control input and disturbance are defined by a piece-wise constant parametrisation $\boldsymbol{u} = [\boldsymbol{u}^{1\top}, \cdots, \boldsymbol{u}^{m\top}, \cdots, \boldsymbol{u}^{M_c\top}]^\top$

18

and $w = [w^{1\top}, \cdots, w^{m\top}, \cdots, w^{M_c\top}]^\top$. Hence, the optimal control problem is rewritten

$$\min_{q^m_{ae_0}, u} \sum_{m=1}^{M_c} \int_{t_{m-1}}^{t_m} V_c^m(q^m_{ae}, u^m) dt \tag{50a}$$

$$\text{s.t.} \quad q^1_{ae_0} = q^c_{ae}, \tag{50b}$$

$$q^{m+1}_{ae_0} = f\left(q^m_{ae_0}, u^m, w^m\right), \quad m = 1, \cdots, M_c - 1, \tag{50c}$$

$$q_{ae_{min}} \le q^m_{ae_f} \le q_{ae_{max}} \quad m = 1, \cdots, M_c, \tag{50d}$$

$$u_{min} \le u \le u_{max}, \tag{50e}$$

where $q^m_{ae_0}$ are the initial conditions of each shooting interval m. Here, $f\left(q^m_{ae_0}, u^m\right)$ denotes the time-integration of the continuous-time system (44) from which $q^{m+1}_{ae_0}$ is found.

As previously stated, the multiple shooting scheme divides the prediction horizon into independent intervals with independent initial conditions $q^m_{ae_0}$ each, which are included in the set of optimisation parameters. In our case, the solution is approached iteratively by steps of a sequential quadratic programming (SQP) [42, ch. 18], which leads to linearisation of continuity constraints (50c), meaning that intermediate solution iterates might be nonphysical and characterised by discontinuities. Also, state inequality constraints are transferred to the final state $q^m_{ae_f}$ of each of the subintervals (50d). One step of the SQP procedure solves for

$$\min_{\Delta p} \Delta p^\top g_i + \frac{1}{2} \Delta p^\top H_i \Delta p \tag{51a}$$

$$\text{s.t.} \quad \Delta q^1_{ae_0} + q^1_{ae_0,i} = q_{ae}, \tag{51b}$$

$$\Delta q^{m+1}_{ae_0} + q^{m+1}_{ae_0,i} = q^m_{ae_f,i} + \frac{d}{dp^m} f\left(q^m_{ae_0}, u^m, w^m\right) \Delta p^m, \quad m = 1, \cdots, M_c - 1, \tag{51c}$$

$$q_{ae_{min}} \le q^m_{ae_f,i} + \frac{d}{dp^m} f\left(q^m_{ae_0}, u^m, w^m\right) \Delta p^m \le q_{ae_{max}} \quad m = 1, \cdots, M_c, \tag{51d}$$

$$u^m_{min} \le u^m_i + \Delta u^m \le u^m_{max}, \tag{51e}$$

where $p^\top = [\cdots, q^m_{ae_0}, \cdots, u^m, \cdots]$ is the set of all optimisation parameters, $q^m_{ae_f} = f\left(q^m_{ae_0}, u^m, w^m\right)$ is the state value at the end of each interval m and the subscript i denotes the current optimisation iterate. This quadratic program is constructed using the gradient g_i and the Hessian, H_i, of the Laplacian of the constrained minimisation problem, $\mathcal{F} + \lambda^\top C$, where $\mathcal{F}$ is the cost function (50a) and $C(q^m_{ae_0}, u^m) \le 0$ is the set of contraints (50c)-(50e), with λ its corresponding multipliers. The Hessian is approximated by the BFGS update formula.
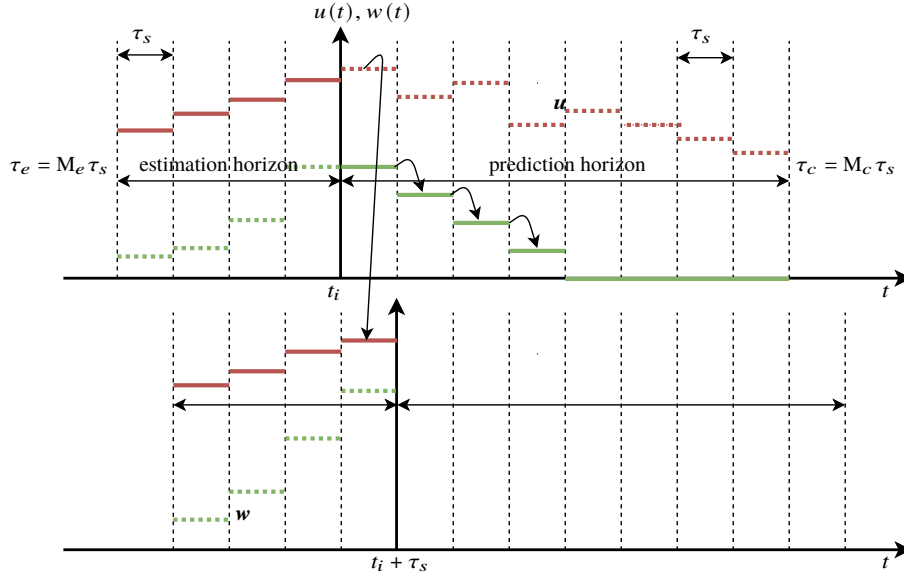
B. MHE and MPC interaction

Fig. 4   MHE/MPC problems in two consecutive sampling times.

The estimator and controller use uniform subintervals of the same length for the multiple shooting parametrisation of the nonlinear problems, which are set equal to the sampling size (i.e., $\tau_s = \tau_c/\mathrm{M}_c = \tau_e/\mathrm{M}_e$), and a piece-wise constant parametrisation for the disturbances and control signals along the subintervals is assumed. To seek optimal computational performance it is further assumed that information is shared between both estimation and control strategies. This is exemplified in Fig. 4, where the assumptions on the information shared between the MHE and the MPC blocks, described in detail in the following lines, are also portrayed. Disturbances and control inputs are depicted using green and red lines, respectively. Solid lines are used to denote the inputs (known information) to each block, and dotted used for the outputs (solutions to the minimisation problems).

Once the MHE problem is solved at a given sampling time, an estimate of the state (used as initial condition in the MPC problem) and of the past disturbance history are obtained. The MPC, however, can further exploit the estimation information by assuming that the disturbance decays linearly over the first $\mathrm{M}_c/2$ subintervals and vanishes over the last $\mathrm{M}_c/2$, as shown in the top of Fig. 4 (note this requires M_c to be an even number). This is done on the assumption that external disturbances do not vanish suddenly so that the MPC can provide an anticipated solution based on a predicted, physically sensible, behaviour of the disturbance.

On the other hand, we assume that the MHE stores information about past control inputs. Hence, once the MPC is solved and the obtained control law is fed back to the system, the first component of the control sequence is transferred to the MHE at the next sampling time, appending it to the last MHE sub-interval while shifting backwards the stored sequence of inputs, as seen in the bottom figure in Fig. 4.

C. Sensitivity analysis

An important advantage of splitting the prediction horizon into small piece-wise continuous-time intervals is that we can make use of analytical adjoints to efficiently evaluate the sensitivities of the system [43]. When applied to our multiple shooting construction it provides us with the derivative of $\mathcal{F}^m$ with respect to $\boldsymbol{p}^m = [\boldsymbol{q}_{ae_0}^{m\top}, \boldsymbol{u}^{m\top}]^\top$, that is the portion $\boldsymbol{g}^m$ of the gradient $\boldsymbol{g}$ used in (51), by

$$\frac{d\mathcal{F}^m}{d\boldsymbol{p}^m} = \int_{t_{m-1}}^{t_m} \left(\frac{\partial V^m}{\partial \boldsymbol{p}^m} + \boldsymbol{\lambda}^{m\top} \frac{\partial \boldsymbol{h}^m}{\partial \boldsymbol{p}^m} \right) dt + [\boldsymbol{\lambda}^{m\top}(t_{m-1}), \boldsymbol{0}], \tag{52}$$

where the zero vector in the last term has $\dim(\boldsymbol{0}) = \dim(\boldsymbol{u}^m)$ and with multipliers $\boldsymbol{\lambda}$ subject to the following ODE and final condition

$$\dot{\boldsymbol{\lambda}}^m = -\frac{\partial \boldsymbol{h}^m}{\partial \boldsymbol{q}_{ae}^m}^\top \boldsymbol{\lambda}^m, \ \boldsymbol{\lambda}^m(t_m) = \boldsymbol{0}. \tag{53}$$

Due to the multiple shooting parametrisation the derivatives can be computed independently at each interval in a parallel implementation. The functional $\boldsymbol{h}^m$ denotes the ODEs (44)–(45) written in implicit form, as in (46).

Relevant terms to solve the adjoint system (53) are easily obtained due to the compact structure of (44):

$$\frac{\partial \boldsymbol{h}^m}{\partial \boldsymbol{q}_{ae}^m} = \begin{bmatrix} 0 & I_{N_m} & 0 & 0 & 0 & 0 \\ q_\infty b^2 D_{q_0} & \Sigma - q_{1l}\Gamma_1^l - \Gamma_1\|\boldsymbol{q}_1 + q_\infty b^2 t_\infty D_{q_1} & \Omega - q_{2l}\Gamma_2^l - \Gamma_2\|\boldsymbol{q}_2 & q_{\xi l}\Gamma_g^l - \Gamma_g\|\boldsymbol{q}_\xi & q_\infty b^2 C_\Gamma & q_\infty b^2 D_\delta \\ 0 & -\Omega + q_{2l}(\Gamma_2^l)^\top & (\Gamma_2)^\top\|\boldsymbol{q}_1 & 0 & 0 & 0 \\ 0 & q_{\xi l}A_\xi^{-1}\Gamma_\xi^l & 0 & A_\xi^{-1}\Gamma_\xi\|\boldsymbol{q}_1 & 0 & 0 \\ t_\infty^{-1} B_{q_0} & B_{q_1} & 0 & 0 & t_\infty^{-1} A_\Gamma & t_\infty^{-1} B_\delta \\ 0 & 0 & 0 & 0 & 0 & 0 \end{bmatrix}, \tag{54}$$

where $\|$ denotes the concatenation operator, which constructs a matrix whose columns are the matrix-vector multiplications between each $\Gamma_\bullet^l$ and $\boldsymbol{q}_\bullet$, that is, $\Gamma_\bullet\|\boldsymbol{q}_\bullet = \left[\Gamma_\bullet^1\boldsymbol{q}_\bullet, \Gamma_\bullet^2\boldsymbol{q}_\bullet, \Gamma_\bullet^3\boldsymbol{q}_\bullet, \cdots\right]$.

Finally, the last interesting term appearing in (52) is

$$\frac{\partial \boldsymbol{h}^m}{\partial \boldsymbol{p}^m} = \begin{bmatrix} 0_{4N_m+2+N_\Gamma} & \begin{matrix} 0 \\ q_\infty b^2 t_\infty D_{\hat{\dot{\delta}}} \\ 0 \\ 0 \\ B_{\hat{\dot{\delta}}} \\ 1 \end{matrix} \end{bmatrix}, \tag{55}$$

where as previously said, we take our control input to be the control surface deflection rate $u(t) = \dot{\delta}_e$. However, other control inputs such as thrust or boundary forcing can be considered by adding the corresponding forcing term $\boldsymbol{\eta}$ in (44) and changing (55) correspondingly. The derivatives involved in the linearisation of the continuity constraints (51c) are obtained using a similar adjoint system to (53) which reads

$$\frac{d\boldsymbol{f}\left(\boldsymbol{q}^m_{ae_0}, \boldsymbol{u}^m\right)}{d\boldsymbol{p}^m} = \int_{t_{m-1}}^{t_m} \lambda^{m\top} \frac{\partial \boldsymbol{h}^m}{\partial \boldsymbol{p}^m} dt + [\lambda^{m\top}(t_{m-1}), 0], \tag{56}$$

with the matrix of multipliers λ^m subject to the ODE and final condition

$$\dot{\lambda}^m = -\frac{\partial \boldsymbol{h}^m}{\partial \boldsymbol{q}^m_{ae}}^\top \lambda^m, \ \lambda^m(t_m) = I_{4N_m+2+N_\Gamma}. \tag{57}$$

The adjoints required for the estimation counterpart are similarly derived, taking into account that $\boldsymbol{w}$ plays the role of $\boldsymbol{u}$ in the previous formulae.

V. Numerical Examples

Two numerical test cases are presented here, after verification of the low-order aeroelastic framework against a well known aeroelastic benchmark, namely the flutter analysis of the Goland wing [44]. The first one introduces a very flexible, high aspect ratio wing used in a gust alleviation control problem. Prior to the control problem, this model will be used to assess the impact of the linearised aerodynamic model on the overall dynamics, comparing several open-loop test cases against solutions obtained with SHARPy [25], which, as previously described, employs a (nonlinear) unsteady vortex lattice method coupled with a geometrically-exact, displacement-based beam model. The second case will put the control framework to the test with a flutter suppression problem of a very flexible wing with faster dynamics.
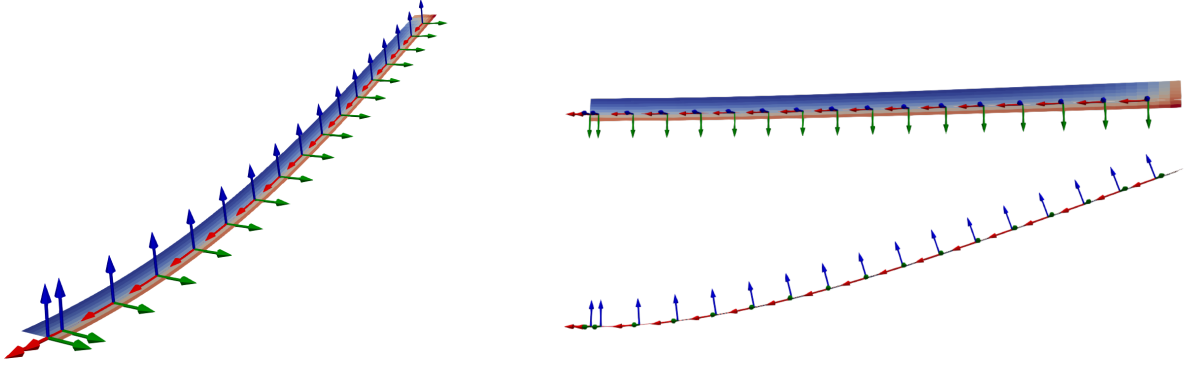
Fig. 5 3D, top and front views of the nonlinear aeroelastic equilibrium deformation. Displayed the local frames of reference x-red, y-green and z-blue.

A. High Aspect Ratio Very Flexible Wing

A very flexible, high aspect ratio clamped wing in a variable speed flow is presented as test bed for the proposed aeroelastic control framework. The objective will be to introduce a gust-load alleviation controller. The wing under test is a modified Goland wing (essentially a longer version, to increase the flexibility of the resulting wing) with geometrical and structural properties outlined in Table 1 and an aileron spanning the outboard 20% of the wing and 50% of the chord for control. An aerodynamic plane of symmetry is imposed on the y-z plane (the wing root) to simulate wall conditions that result in the lack of three dimensional effects at the wing root. The global frame of reference is located at the wing root and any angles specified will be defined at this point; local, body-attached frames are shown in Fig. 5 about which structural properties are defined. Note that aerodynamic sections are assumed to rotate rigidly about the elastic axis (i.e. there is no chordwise deformation in the aerodynamic surface).

Table 1 High aspect ratio, flexible wing properties

Span	L	45.72 m
Chord	$2b$	1.8288 m
Mass per unit length	μ	20.71 kg/m
Mass moments of inertia per unit length	I_{xx}	8.64 kg m
	I_{yy}	0.86 kg m
	I_{zz}	7.77 kg m
Out-of-plane bending stiffness	EI_{yy}	9.77 MN m^2
In-plane bending stiffness	EI_{zz}	977 MN m^2
Torsional stiffness	GJ	98.7 MN m^2
Axial stiffness	EA	1 MN
Shear stiffness	GA	10 MN
Centre of mass offset (in body-attached FOR)	r_{cm}	$[0, -0.1829, 0]^\top$ m
Elastic axis from leading edge (in body-attached FOR)	r_{ea}	$[0, -0.6035, 0]^\top$ m

The aerodynamic model employed in the MHE/MPC framework will be based on the system obtained linearising

the SHARPy nonlinear UVLM reference with a prescribed wake model about the undeformed wing with 5 degrees angle of attack. The aerodynamic inputs and outputs are projected onto the structural coordinates with the addition of three inputs: the aileron deflection, aileron deflection rate and external flow vertical velocity at the leading edge. The resulting state-space is similar to that depicted in Fig. 2, where G_{gust} represents a gust system that convects the single gust input defined at the leading edge downstream to the rest of the wing and propagates it uniformly across the span.

A suitable discretisation for the aerodynamic grid and structural elements has been found by measuring the wing tip deflection and total aerodynamic forces from the SHARPy model until measurements converged, which resulted in a model discretised with 8 panels in chord, 64 panels in span (resulting in 32 structural beam elements) and an 80-panel wake (i.e. a 10-chord wake length). This equates to a linear system with 13321 states, including the gust system states. It is clear how this system is not suitable for control applications due to its large size, so a Krylov-subspace model order reduction is performed to reduce it to a manageable size for control purposes.

The Krylov-subspace ROM is obtained interpolating at the DC gain (steady-state) and only interpolating once to reduce the number of factorisations required. Contrary to the Goland wing case [44], the input-output dimensionality of the current case is much larger, with 27 inputs and 12 outputs (the first twelve structural modes are used to construct the modal-based system), so even when the Krylov subspace order is reduced, the resulting ROM is of considerable size. However, to exploit the fact that the number of outputs is considerably smaller than the number of inputs, we can construct a single Krylov subspace on the observability side to obtain a single projector matrix $\boldsymbol{Z}$ using (40). Since this matrix is orthogonal, we can take $\boldsymbol{V} = \boldsymbol{Z}^{\top}$ and build the ROM as in (41). The result of building this ROM with a 3rd-order ($r_c = 3$) Krylov-subspace is a stable realisation with 36 states.

Prior to analysing the control problem, it is worth evaluating the impact, both structural and aerodynamic, that nonlinearities have on a wing capable of deforming significantly, and whether it is appropriate to use linear models as part of the MHE/MPC framework for these type of problems. Therefore, using SHARPy, the full nonlinear problem (nonlinear aerodynamics and structure) is compared against three modal-based low-order models (17) constructed with the beam's first 12 natural modes, with varying degree of nonlinearity, all coupled with the same reduced aerodynamic model linearised around an undeformed initial condition. The three structural models and the associated acronym used in results and figures consist of: i) a fully linearised model (17) around the undeformed configuration and linearised displacements equation (35) (L struct), ii) a linearised model (17) around the undeformed configuration retaining the kinematic nonlinear couplings i.e. the rotation/displacement equations (8) and (35) (herein referred to as semi-linear, SL struct) and iii) the original modal-based nonlinear model (17) and rotation/displacement equations (8) and (35) (NL struct). These are subject to three dynamic tests to evaluate the validity of the linear aerodynamics: a release from the undeformed initial condition at a 5° angle of attack at different air speeds (without gravitational forces), an external vertical velocity input and an aileron input (both with gravity effects). The last two start from the nonlinear equilibrium condition in a 30 m/s wind with the clamped root section at 5° angle of attack – the deformed equilibrium state. All test

24

cases that employ reduced linear aerodynamics use the same system that is linearised about the undeformed condition and defined in non-dimensional time. Consequently, the only parameters that vary are the scaling terms that depend on the dynamic pressure in (44).

1. Dynamic response of the wing released at different free stream velocities without gravity effects
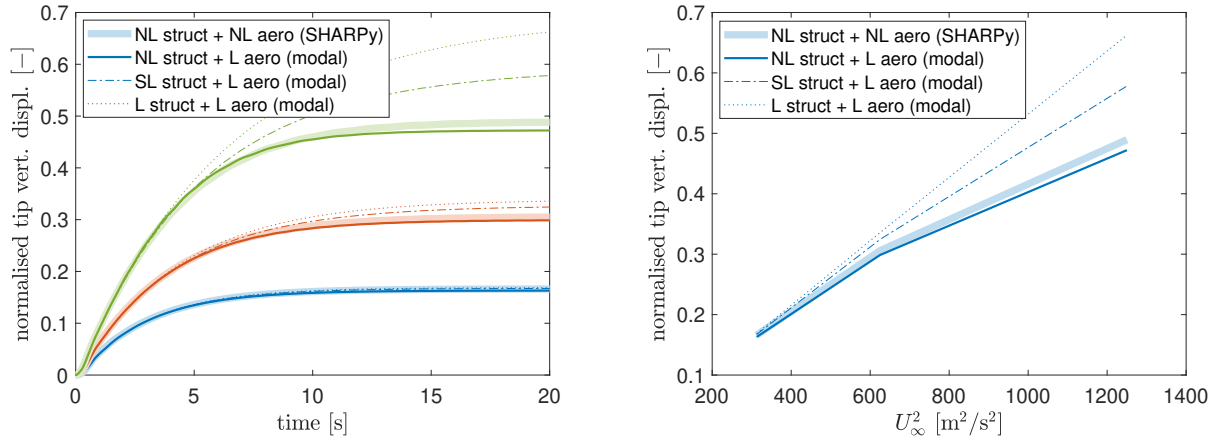

Fig. 6 Dynamic response (left) of the wing release at three different free stream velocities. Steady state values against velocity squared shown on the right.

Fig. 6 shows the vertical wing tip displacement over time when the wing is released from the undeformed condition at 5° angle of attack at three different free stream velocities: 17.67 m/s, 25.00 m/s and 35.35 m/s (blue, red and green in Fig. 6). This corresponds to a doubling in dynamic pressure (with constant density $\rho = 1.02\,\mathrm{kg/m^3}$) at each step to visualise the effects of nonlinearity with greater ease. At the lowest velocity, all models show a steady-state wing tip displacement approaching a vertical displacement of 17% span, matching well the SHARPy nonlinear reference response. However, as velocity is increased to double and quadruple the initial dynamic pressure, the discrepancy is most apparent in the linear structural models. Fig. 6 also shows the static equilibrium wing tip position from where it is clear how the nonlinear structural models differ from the linear trend established by the fully linearised model as dynamic pressure is increased.

Since all but SHARPy employ the same linear aerodynamics, it is clear that the greatest source of error emanates from the use of a linear structural model, unable to capture important physics such as the follower force effects as the wing deforms. On the other hand, the case with the nonlinear structural model shows very good agreement compared to the SHARPy reference. Only a small underestimation of the deflection is observed at the highest speed where the wing deforms to a considerable 48% of span (the deformed wing in these conditions was shown in Fig. 5) despite the use of linear aerodynamics. Since this case employs a nonlinear structural model, the discrepancies between it and SHARPy can be attributed solely to the differences between linear and nonlinear aerodynamics. This is supported by

structural-only comparisons between the nonlinear modal-based structural model and SHARPy's structural model that have shown excellent comparisons [45].

The linear aerodynamic model differs with its nonlinear counterpart in the assumption of small perturbations to the grid coordinates such that the aerodynamic influence coefficients (AICs) become constant and the wake frozen in shape. In the nonlinear case in which AICs change as the wing deforms, the influence that bound panels have on each other changes. Under significant nonlinear deformation, the greatest variations in geometry are most obvious in a global sense, where, for instance, the distance between root and tip panels is reduced. However, since the influence between panels is governed by the Biot-Savart law, inversely proportional to the distance squared, the differences become negligible. On the contrary, the linearised formulation would impose a heavier penalty on systems with large local deformations, unlike the present case (Fig. 5). Therefore, it is unlikely that the linearisation of the UVLM formulation is directly responsible for the mismatch.

The small differences observed at 35 m/s in Fig. 6 are due to the negative twist deformation (washout) that the wing experiences and its effect (a reduction in lift) being more notable in the linear case. The reason behind this resides in the use of linear projectors to map the position and rotation of the structural nodes onto the aerodynamic grid coordinates. The linear transformation K_v in Fig. 2 causes an effective change of chord length at a particular section when the beam is twisted. In other words, the linear rotation of a section results in a projection of the chord, increasing its effective length and therefore generating more lift, effect that would scale linearly with the twist angle. Nonetheless, this error that results from the linearised aerodynamic model at significant deformations is below 4% of the span, which justifies its use as a controller model.

2. Input-output dynamic tests with gravity effects

The remaining two tests explore how well the aeroelastic response is captured by the reduced linear aerodynamic system in comparison to the SHARPy reference when the system is excited by an external vertical gust or an aileron input. Fig. 7 shows the wing tip vertical displacement over time for the two cases, both starting from the equilibrium condition when the root section is clamped at 5° in a 30 m/s wind. The vertical gust profile consists of a 2 s ramp to −3 m/s and constant thereafter. Similarly, the aileron input is a 2 s ramp to a −5° deflection (positive downwards) that is then held constant. Again, the comparison between the two models which differ particularly in the aerodynamics shows a very similar deflection, with the reduced model capturing well both the transient and steady-state response. This is of particular importance in maintaining the assumption that reduced linear aerodynamics can be used as representative model for control, since the effect of both external disturbances and aileron inputs are very well matched when compared to the nonlinear, full-order UVLM even when the wing experiences significant deflection. Finally, the smoothness and damping of the response are worth a note. Both with linear and nonlinear aerodynamics, the introduction of external inputs do not excite any higher-order structural modes and the bending response is significantly over-damped. These

slow dynamics are likely attributed to the wing's large inertia requiring a significant disturbance to excite higher-order modes and beneficial for the control problem, since a larger sampling time may be sufficient to capture the relevant dynamics.
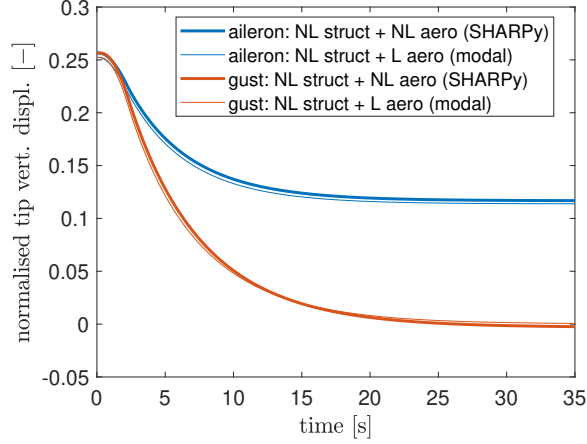

Fig. 7 Comparison of the wing's dynamic response to external gust and aileron inputs with SHARPy's nonlinear reference.

From these tests it is clear that using a reduced, linear aerodynamic model is not detrimental in capturing the dynamic aeroelastic response of a very flexible wing, provided that the structural model is capable of capturing the geometric nonlinearities present. Removing them from the structural description produces significant mismatch with respect to the full nonlinear model, whereas the choice of a linear aerodynamic model introduces only small errors even when deflections are significant when compared to the linearisation state. Hence, our assumption that the linear aerodynamic model coupled with the modal-based nonlinear structural model can be used as part of a model predictive control framework to control structures with considerable deformations is maintained and will be demonstrated in the following section.

3. Estimation and control in a gust alleviation problem

The previously described wing, with structural properties gathered in Table 1, is now used in a gust-load alleviation (GLA) problem set-up, where the nonlinear estimation and control strategies described in § IV are employed. The wing, with a root angle of attack of 5°, is initially at equilibrium in a flow with airspeed $U_\infty = 25$ m/s in the positive y-axis of the global frame of reference (see Fig. 5) and density $\rho = 1.02$ kg/m^3. The external forces are gravity, which acts along the negative z-axis of the global frame of reference, and a $1 - \cos$ shaped gust

$$w_g(t) = \frac{W}{2}\left(1 - \cos\left(\frac{\pi U_\infty(t - t_g)}{H_g}\right)\right)\left(\mathcal{H}\left(t_g\right) - \mathcal{H}\left(t_g + \frac{2H_g}{U_\infty}\right)\right), \tag{58}$$

27

which reaches the wing root leading edge at $t_g = 0.1$s, with intensity $W = 2$ m/s, span $H_g = 90$ m and $\mathcal{H}(t)$ denoting the Heaviside step function at time t.

Both the estimator and controller employ the nonlinear low-order model (44), equipped with the first 12 modes (ordered in ascending natural frequency) of the structure. The aerodynamic model corresponds to the reduced order model of the linearised UVLM at a $5°$ angle of attack configuration, as described in the previous section. On the other hand, we use a finite element discretisation of the nonlinear intrinsic equations (1)–(2), similar to the one described in [46], to model the controlled system's structural dynamics plus linearisation of a UVLM, which uses the FE solution as nodal inputs and has undergone a mild model reduction process. This is done to ease and speed up the simulation of the controlled system, since the resulting UVLM has a size of the order $O(10^4)$. This model already provides us with sufficient plant-model mismatch to assess the performance and robustness of both the estimation and control strategies.

The open-loop nonlinear optimal control problems (46) and (48) are solved until the Karush–Kuhn–Tucker (KKT) conditions are satisfied with a tolerance of 10^{-4} and 10^{-5} (for the MHE and MPC problems, respectively). Three different control scenarios have been considered, to showcase diverse optimisation parameters. The first case uses a sampling period of $\tau_s = 0.25$ s with $M_e = 12$ and $M_c = 24$ with input constraints $u_{max} = -u_{min} = 10°/s$ and state constraints (deflection angle) $q_{\delta_{max}} = -q_{\delta_{min}} = 5°$. To assess the effect on performance of control saturation, the second case is set up with the exact same parameters as the first one except for no constraints on the deflection rate or angle. The chosen sampling period is of the order of a fifth of the period associated to the third and fourth natural modes of the structure (with frequencies of 1.14 and 1.20 Hz). This rather small sampling time should increase robustness of the controller/estimator in front of model mismatch errors. The estimator horizon is of the order of a half the period of the first mode (bending), with a frequency of 0.18 Hz, while the control horizon is of the same order of this low frequency mode. These are deemed to be sufficient for successful estimation and control performance, as suggested by the numerical findings. Finally, a third case, with no control saturation and where the sampling time has been doubled is considered to show the control performance sensitivity with respect to the latter parameter.

In all cases the MHE receives measurements of the translational velocities at four different stations of the wing, $0.25L$, $0.5L$, $0.75L$ and L, with weighting matrix Q_e equal to the identity, while the MPC penalises the perturbed energy of the system with respect to the static deformed configuration by setting $Q_c = \mathrm{blkdiag}(0_{N_m}, I_{N_m}, I_{N_m}, 0_{N_m+1}, 0_{N_\Gamma}, 0)$ and $\boldsymbol{q}_r$ the equilibrium point of (44) at $U_\infty = 25$ m/s.

Fig. 8 shows the vertical displacement as a fraction of the wing span and the wing root bending moment normalised with the value at static initial equilibrium (-99.79 kNm) for the three different controlled scenarios and the uncontrolled case. As observed, in the uncontrolled case the gust causes the wing tip to experience a deflection 2.27 times that of the static equilibrium. All control cases achieve successful reduction in the deflection, with the faster, no-saturation, case virtually suppressing it. It is also revealed that increasing the sampling time reduces the suppression performance. Regarding the root bending moment, a key metric in gust load alleviation, the gust produces a maximum moment of
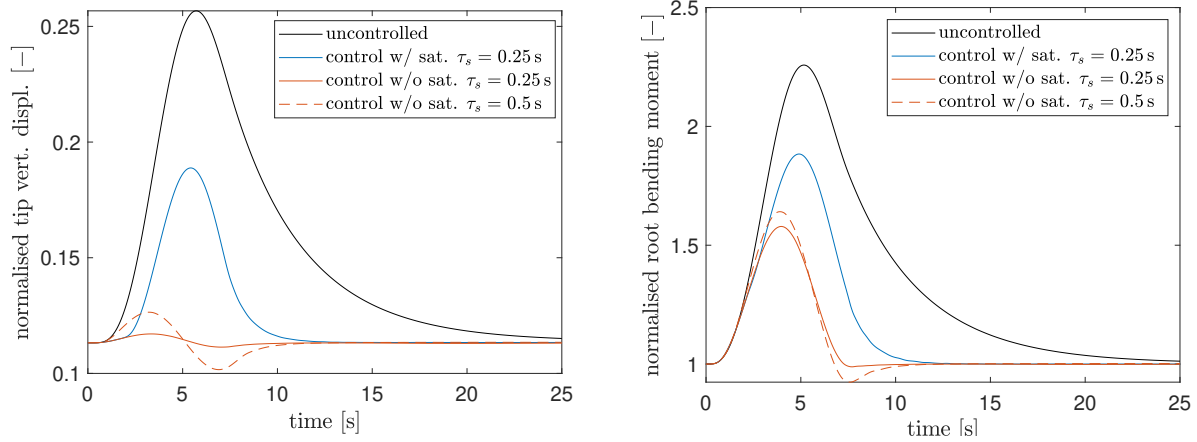
Fig. 8   Normalised wing tip vertical displacement (left) and root bending moment (right).
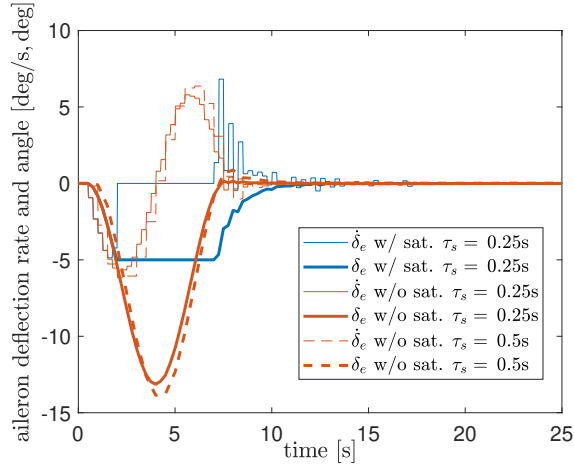

Fig. 9   Aileron deflection rate (control input) and deflection angle.

2.26 times that of the static equilibrium. Again, both the saturation and unconstrained control scenarios reduce notably the load at the root, respectively a 16.61% and 30.35% peak load reduction (a slightly lower 27.40% for the slower controller), but most importantly they shrink the time the wing is being overloaded.

The corresponding control inputs are gathered in Fig. 9, where the blue lines belong to the case with saturation, where the aileron deflection angle reaches its minimum allowed deflection, and the red to the unconstrained ones (dashed lines corresponding to the slower control case). These commands would hardly be reproduced by conventional control strategies such as, for example, a PID controller. For a PID controller, the response is a reaction to some chosen measurement and highly sensitive to the local placement of the sensor. For instance, in the unconstrained case, we see that our method, using knowledge of the system's physics and penalising globally the perturbed energy of the system, is able to virtually suppress the wing tip-displacement, as shown in 14. If a PID controller was employed, measuring the wing-tip vertical velocity, such a reduction would not be possible since measurements would be nearly zero and no

control would be applied. If strains were to be used to feed the PID instead, the controller would need very fine tuning to not overreact (since strains are rather high even when the wing's displacements are negligible). Another important advantage is that MHE and MPC parameters are less case-dependent, and similar outcomes using the same set-up should be expected for gusts of varying intensities and spans. Moreover, constraints in the control inputs are seamlessly embedded in the optimal control problems, while their addition to other control techniques may result in less elegant and rather cumbersome approaches.

B. Pazy Wing

The Pazy wing [47] shown in Fig. 10 is a very flexible wing model designed as an aeroelastic benchmark case that inspires the demonstrator for the proposed control framework. The original wing, conceived to be tested in a wind tunnel, is 55 cm in span and 10 cm in chord and consists of a rectangular aluminium spar with evenly spaced Nylon ribs with a NACA0018 airfoil profile. An Oralight skin covering the ribs gives the wing its aerodynamic shape. Finally, a Nylon wing tip rod is fitted to modify the wing dynamics and reduce the first torsional mode's frequency. The control problem at hand employs the first version of the wing model, which consists of a beam model with constant spanwise stiffness and inertia properties that are listed in Tables 2, 3 and 4. The frame of reference in which these properties are expressed corresponds to x being along the beam reference line positive outboard, z pointing upward and y completing the set. A simulated aileron is fitted on the outboard 20% of span and 50% chord that will be used as the control input. Later iterations of the Pazy wing model have been explored by the authors in [48].

Fig. 10   Pazy wing experimental model.

Table 2   Beam model stiffness matrix.

Axial stiffness	EA	7.16 MN
Out-of-plane shear stiffness	GA_y	1 MN
In-plane shear stiffness	GA_z	3.31 MN
Torsional stiffness	GJ	7.2 N m^2
Out-of-plane bending stiffness	EI_{yy}	4.67 N m^2
In-plane bending stiffness	EI_{zz}	3.31 kN m^2

The stability analysis of this constant-properties version of the wing shows that the dynamic stability is dependent

Table 3   Beam model mass and geometrical properties.

Span	L	0.55 m
Chord	$2b$	0.1 m
Elastic axis reference line	$y_{ea}/(2b)$	0.0
Leading edge line	$y_{le}/(2b)$	0.4475
Centre of gravity line	$y_{cg}/(2b)$	-3.5×10^{-3}
Mass per unit length		0.55 kg/m
Inertia per unit length	I_{xx}	3.030×10^{-4} kg m
	I_{yy}	1.515×10^{-4} kg m
	I_{zz}	3.636×10^{-3} kg m

Table 4   Wing tip rod mass and inertia properties.

Position	r_b	$[0.555, -0.005, 0]$ m
Mass	m_{rod}	19.95 g
Inertia	I_{xx}	1.2815×10^{-4} kg m^2
	I_{yy}	2.87×10^{-7} kg m^2
	I_{zz}	1.17×10^{-4} kg m^2

on the wing deflection, which in open-loop conditions is a unique function of the angle of attack and the dynamic pressure. The results in Fig. 11 show that the flutter speed decreases with angle of attack because of the increased wing deflection. In the frequency plot in Fig. 11a it is illustrated how flutter occurs at the coalescence of the first torsion and second out-of-plane bending modes, an event that is brought forward by larger deformations which are driven by an increase in angle of attack. However, the first flutter mode can be stabilised by further increasing the deflection. In open-loop, for a given angle of attack this can be achieved by increasing the free stream velocity, which leads to the "hump" in positive damping ratio seen in the V-g plot. To further explore the relation between stability and deflection, Fig. 12 shows the stability boundaries for different deflections and velocities. The region of instability of the first flutter mode is clearly seen and also how that mode becomes stable after a certain deflection. The instability seen at larger deformations corresponds to the first torsion and first bending flutter mode, that has a much higher onset of instability speed. This dependency of flutter on the wing deformation can be used as leverage by the controller as, in closed-loop, the aileron can be used to change the deflection of the wing to alter the stability properties, which on Fig. 12 would correspond to moving in a roughly horizontal line (for a constant velocity).

As indicated by the stability analysis results, this wing makes for a compelling flutter-suppression problem, where both the nonlinear estimation and control strategies described in § IV are put to the test. The wing is released from the undeformed configuration with a root angle of attack of 4° in a uniform flow with airspeed $U_\infty = 50$ m/s and density $\rho = 1.225$ kg/m^3. Besides the aerodynamic forcing, the other actuating external force is gravity. As shown in Fig. 11 and Fig. 12, such an airspeed places the wing within the first unstable regime, and soon after its release (from around $t > 0.5$ s) flutter starts to develop. It is then that the control framework (nonlinear MHE and MPC) is switched on.
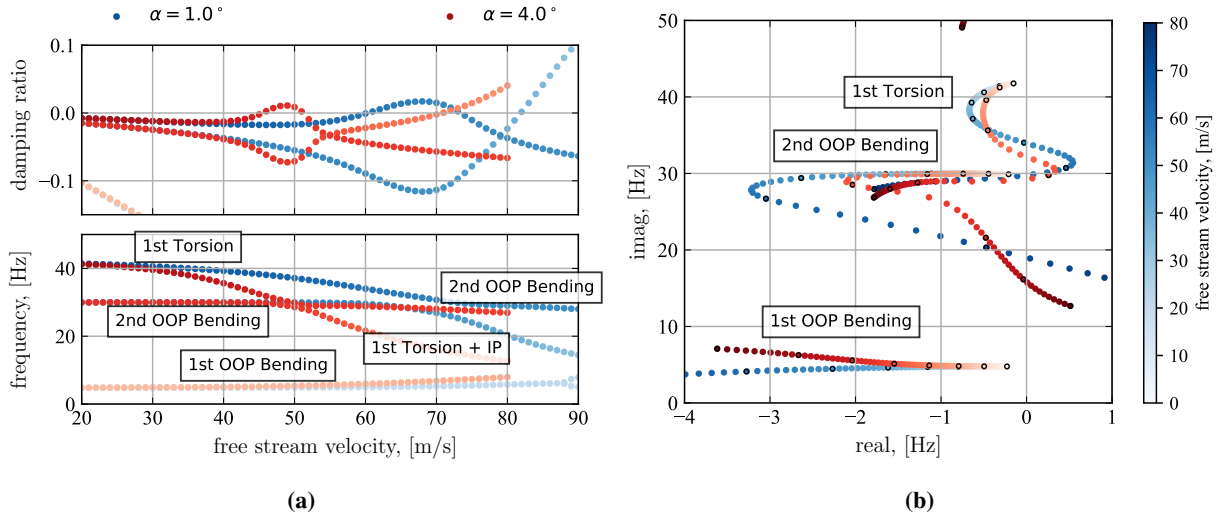
Fig. 11 Stability analysis of the wing with (a) stability plot at two non-zero angles of attack and (b) root locus diagram.
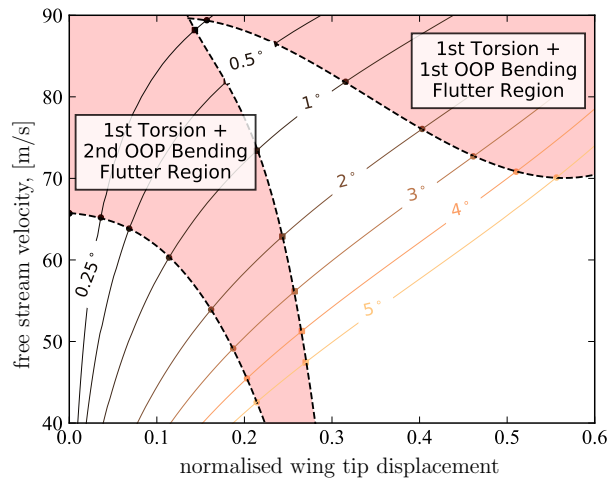

Fig. 12 Wing flutter instability regions.

The model used within the estimation and control strategies is the modal-based system (44), constructed with 9 modes: the first three out-of-plane bending, the first three torsion, the first two in-plane bending and the first axial modes of the structure. The aerodynamic model corresponds to the reduced order model of the linearised UVLM at a $4°$ angle of attack configuration, following the previously described process. The original UVLM employs a spanwise discretisation using 128 nodes, a chordwise discretisation which divides the chord into 8 intervals and a wake extending 8 chord lengths, resulting in a system with 11,273 states: this is unmanageable for NMPC/NMHE. Similarly to the control cases with the previous wing model, we set up the closed-loop control problem using a finite element discretisation of the nonlinear intrinsic equations (1)–(2) to model the controlled system's structural dynamics coupled to a full-order linearisation of the UVLM.

As shown in the following two subsections, by slightly modifying the control parameters the controller aims to suppress oscillations induced by flutter via two completely distinct actuation mechanisms: while the first one opts for the more obvious response where the aileron is deflected in an oscillatory manner to directly counteract flutter, the second one consists of a less evident response where the aileron's aim is to increase the wing's deformation to take it outside of the unstable region, where the controller's knowledge of the wing's stability around nonlinear equilibria is exploited. In both set of results the open-loop nonlinear optimal control problems (46) and (48) are solved until the KKT conditions are satisfied with a tolerance of 10^{-4} for both the MHE and MPC problems. The discrete-time counterpart formulation of the MPC and MHE definitions of (46) and (48) has been employed to obtain the following results. Abusing notation, the same nomenclature is used to define the weighting matrices defining the cost functions.

1. Flutter suppression via direct actuation

In this case, both the estimation and control problems are set up with a rather small sampling time of $\tau_s = 0.0025$ s ($\approx$ 0.075 times the flutter oscillation period, τ_f), with equal estimation and control horizons of $\tau_e = \tau_c = 0.06$ s ($\approx 1.8\tau_f$). Similarly to the previous GLA problem, involving the high-aspect ratio wing, the MHE measures the translational velocities at four different stations of the wing: $0.25L$, $0.5L$, $0.75L$ and L, with weighting matrix $Q_e = 0.1I$. Here, the cost function of the MHE optimisation problem (48) is enhanced by adding a penalty term $\|\boldsymbol{q}_{ae}^e - \boldsymbol{q}_{ae,r}^e\|_{P_e}$. The vector $\boldsymbol{q}_{ae}^e$ is the initial condition for the estimation window and $\boldsymbol{q}_{ae,r}$ is a reference state which is initialised as the static equilibrium for the given flow conditions and updated at any other sampling point with the state at the start of the second sub-interval of the previous MHE solution. This is done to improve initial convergence of the estimation problem, since extra information of the reference configuration around which flutter-induced oscillations occur is given, and also of the subsequent ones, since the information of the previous estimations can be exploited. The weighting matrix for this extra term is $P_e = \text{blkdiag}(I_{N_m}, 0_{N_m}, I_{N_m}, I_{N_m+1}, I_{N_\Gamma}, 1)$, which penalises deviations on all the states except for the velocities, which due to flutter, are subject to large variations. To suppress flutter oscillations, the MPC's cost function only places a penalty on velocity, with $Q_c = \text{blkdiag}(0_{N_m}, I_{N_m}, 0_{N_m}, 0_{N_m+1}, 0_{N_\Gamma}, 0)$ and two different control constraints on aileron deflection have been explored: a stricter constraint of $q_{\delta_{\max}} = -q_{\delta_{\min}} = 5°$ and a more permissive one of $q_{\delta_{\max}} = -q_{\delta_{\min}} = 15°$.

With this choice of parameters, the controller's actuation is an oscillatory one as seen in Fig. 13, where the flap is deflected synchronously to the flutter vibrations in order to directly counteract its effect. In both cases, the controller reaches the aileron deflection saturation limits, capping the actuation in the more tightly constrained case a more prolonged time, as clearly seen in the bottom plot of Fig. 13. The outcome of both control inputs is a wing which experiments a transition from the free flutter oscillations to a forced response driven by the flap actuation, where oscillations are intensified during the few instants following the controller's activation at $t = 0.15$ s in Fig. 13, and with a final substantial reduction in the flutter oscillations: a decrease of over an 80% in the amplitude of the wing-tip vertical
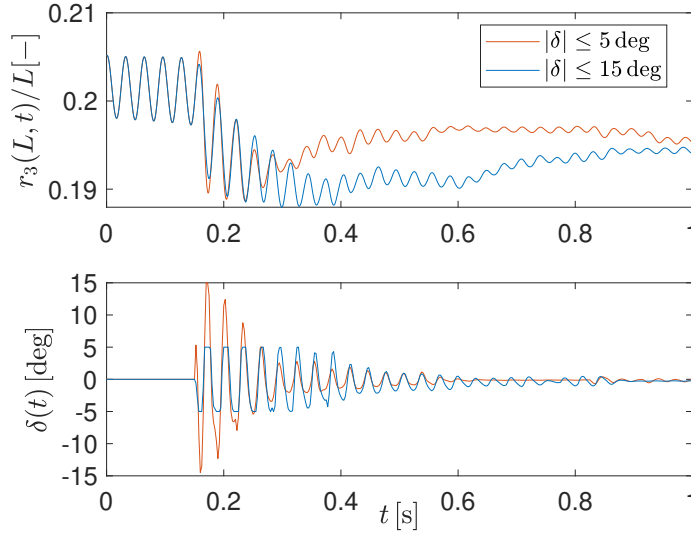
Fig. 13 Normalised wing tip displacement and aileron deflection vs time for the flutter suppression direct actuation mechanism.

deflection, in both saturation cases, is obtained. Where stricter saturation limits are applied, the transition oscillations are milder but get prolonged over a longer period of time. Due to the plant-model mismatch, the controller is observed to react occasionally after the main suppression is achieved (e.g. at around $t = 0.85$ s) in both cases, however showing a robust behaviour throughout the simulated time window.

2. Flutter suppression via deformation control

For this second flutter suppression case, the estimation/control framework uses a longer sampling time of $\tau_s = 0.01$ s (≈ 0.33 times the flutter oscillation period, τ_f), with an estimation horizon of $\tau_e = 0.12$ s ($\approx 3.6\tau_f$). Three different values for the prediction horizon have been explored, ranging from $\tau_e = 0.12$ s ($\approx 3.6\tau_f$) to $\tau_e = 0.48$ s ($\approx 14.4\tau_f$). The MHE measures the same variables as in the previous case with identical additional penalty term $\|q_{ae} - q_{ae,r}^e\|_{P_e}$. Here, the MPC also penalises the velocity states only, with $Q_c = \text{blkdiag}(0_{N_m}, I_{N_m}, 0_{N_m}, 0_{N_m+1}, 0_{N_\Gamma}, 0)$, but an additional terminal penalty $\|q_{ae}(t_i + \tau_c) - q_{ae,r}\|_{P_c}$ with $P_c = 5Q_c$. Control constraints on aileron deflection and deflection rate of $q_{\delta_{\max}} = -q_{\delta_{\min}} = 15°$ and $u_{\max} = -u_{\min} = 100°/s$ are placed with mild actuation penalty $R_c = 0.01$.

With this set of parameters, characterised by a longer prediction horizon than the previous test case, a higher penalty on the velocity states at the end of the prediction horizon and a light actuation penalty, the controller opts for an alternative minimum consisting of changing the deformation state of the wing to configurations where the initial flutter instability is replaced by a configuration where flutter does not occur and aerodynamics are more dissipative, which favours the control purpose of dampening out the residual oscillations.

As seen in Fig. 14a, for the longest prediction horizon case, the flap is deflected in a rather smooth way from an initial

0 angle to a constant final angle of 9.2°. This leads to the wing increasing its deformation gradually until it stabilises at a normalised wing tip deflection of 31% (see Fig. 14b) while experiencing some oscillations during the transient period (from $t = 0.2$ to $t = 0.4$ s in Fig. 14a) which die out fairly rapidly thanks to the increased aerodynamic damping acting on such deformed regime. As the prediction horizon is shrunken, a change in the MPC's target local minimum is observed, as shown by the red and blue lines of Fig. 14a, where the closed-loop response is now a wing moving towards a less deformed state, achieved by a negative aileron deflection, which effectively brings the structure outside the instability region too (note how for $U_\infty = 50$ m/s escaping the unstable region can be achieved by either moving horizontally to the left or to the right). The rationale behind this change in the response is not trivial, and to avoid this bistable closed-loop response a further penalty on larger/smaller deformations might be considered. It is observed, however, that when the prediction horizon is long enough less actuation is required, as suggested by a less oscillatory flap deflection rate in Fig. 14a since aerodynamic damping is given more time to damp out the remaining oscillations. For shorter predictive horizons, this damping has less effect and a more oscillatory response of the controller is required to attenuate vibrations throughout the transient response.

This set of results is indeed very remarkable, since the controller's ability to predict the different stability regions arising from varying levels of deformation, leveraging the full-nonlinear simulations that underpin the framework, is highlighted. Even control approaches, based on successive linearisations around instantaneous configurations, which are usually labelled as nonlinear control strategies too, would not be able to recreate such a response. This case demonstrates, again, that despite the use of linear aerodynamics, the main nonlinear phenomena that is present in the dynamics of aeroelastic systems is successfully captured by the modal-based system and hence it provides a very suitable model to underpin nonlinear MHE and MPC strategies.
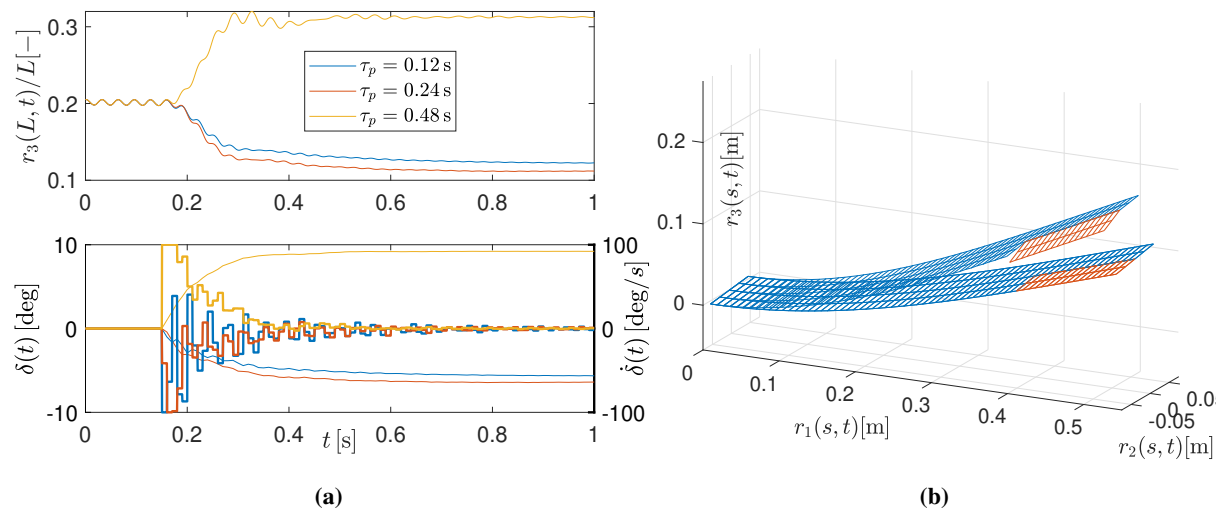

Fig. 14   (a) Normalised wing tip displacement, aileron deflection and rate for the deformation-control-based mechanism and (b) 3D view of the initial and final wing configurations.

VI. Conclusions

In this paper we have presented a low-order nonlinear aeroelastic model, which retains structural geometrically nonlinear effects inherited from the intrinsic geometrically-exact beam equations and employs a linearised UVLM, projected onto the structural modal expansion. This yields a very compact model, with quadratic nonlinearities, amenable to model-based estimation and control strategies. Further, numerical examples have been shown to support the claim that linear aerodynamic formulations are able to produce satisfactory and accurate predictions as long as they are employed together with a nonlinear structural formulation, able to account for follower force effects and changes in the overall dynamics of the structures due to large deflections, as exemplified by the last flutter suppression test-case, where the controllers knowledge of the nonlinear stability is crucial.

The accuracy of this low-order model has been proven to be sufficient to underpin both (nonlinear) moving horizon estimation and model predictive control strategies. Most importantly, this has been attained using very few structural modes (12 for the results in §V.A and 9 for those in §V.B) and a massively reduced aerodynamic model (from 13,321 to 36 states in §V.A and a reduction from 11,273 to 54 states in §V.B). This paves the way, for the first time, to estimate and control nonlinear aeroelastic systems undergoing large deflections, in real-time.

Future investigation will focus on two main items: i) Work towards real-time application. For relatively slow dynamical systems (such as very flexible HALE-type aircraft) it is virtually possible to run the control framework online, since the execution time of the MHE/MPC nonlinear problem iterations are well below the sampling period, even with the current Matlab implementation. However, to achieve maximum performance compiled programming languages and/or dedicated-software strategies should be used. The application of a sub-optimal MPC and MHE strategy, where the nonlinear problems are not iterated until convergence at each of the sampling points, such as a *real-time iteration* [22] alike procedure, could be also considered to contribute towards this objective. ii) Application of the estimation-control framework to the full nonlinear simulations of free-flying vehicles, including rigid-body motions in our low-order model (done in a straightforward manner using the intrinsic description) to ultimately provide real-time control and estimation for very flexible aircraft-like structures.

Acknowledgements

References

[1] A. Colozza. Analex Corporation. NASA, "Initial Feasibility Assessment of a High Altitude Long Endurance Airship," 2009. Available online: https://ntrs.nasa.gov/archive/nasa/casi.ntrs.nasa.gov/20040021326.pdf [Accessed on 06/06/2019].

[2] d'Oliveira, F. A., de Melo, F. C. L., and Devezas, T. C., "High-Altitude Platforms - Present Situation and Technology Trends," *Journal of Aerospace Technology and Management*, Vol. 8, No. 3, 2016, pp. 249–262.

[3] Patil, M. J., and Hodges, D. H., "Output Feedback Control of the Nonlinear Aeroelastic Response of a Slender Wing," *Journal of Guidance, Control, and Dynamics*, Vol. 25, No. 2, 2002, pp. 302–308. doi:https://doi.org/10.2514/2.4882.

[4] Dillsaver, M., Cesnik, C., and Kolmanovsky, I., "Gust Load Alleviation Control for Very Flexible Aircraft," *AIAA Atmospheric Flight Mechanics Conference*, Portland, OR, 2011. doi:https://doi.org/10.2514/6.2011-6368.

[5] Gibson, T., Annaswamy, A., and Lavretsky, E., "Modeling for Control of Very Flexible Aircraft," *AIAA Guidance, Navigation, and Control Conference*, Portland, OR, 2011. doi:https://doi.org/10.2514/6.2011-6202.

[6] Dillsaver, M., Cesnik, C. E., and Kolmanovsky, I., "Trajectory Control of Very Flexible Aircraft with Gust Disturbance," *AIAA Atmospheric Flight Mechanics (AFM) Conference*, Boston, MA, 2013. doi:https://doi.org/10.2514/6.2013-4745.

[7] de F.V. Pereira, M., Kolmanovsky, I., and Cesnik, C. E. S., "Model Predictive Control with Constraint Aggregation Applied to Conventional and Very Flexible Aircraft*," *2019 IEEE 58th Conference on Decision and Control (CDC)*, 2019, pp. 431–437. doi:https://doi.org/10.1109/CDC40024.2019.9029769.

[8] Haghighat, S., T. Liu, H. H., and R. A. Martins, J. R., "Model-Predictive Gust Load Alleviation Controller for a Highly Flexible Aircraft," *Journal of Guidance, Control, and Dynamics*, Vol. 35, No. 6, 2012, pp. 1751–1766. doi:https://doi.org/10.2514/1.57013.

[9] Pereira, M., Kolmanovsky, I., Cesnik, C. E., and Vetrano, F., "Model Predictive Control Architectures for Maneuver Load Alleviation in Very Flexible Aircraft," *AIAA Scitech 2019 Forum*, San Diego, CA, 2019. doi:https://doi.org/10.2514/6.2019-1591.

[10] Simpson, R. J., Palacios, R., Hesse, H., and Goulart, P., "Predictive Control for Alleviation of Gust Loads on Very Flexible Aircraft," *55th AIAA/ASME/ASCE/AHS/ASC Structures, Structural Dynamics, and Materials Conference*, National Harbour, MD, 2014. doi:https://doi.org/10.2514/6.2014-0843.

[11] Wang, Y., Wynn, A., and Palacios, R., "Nonlinear Aeroelastic Control of Very Flexible Aircraft Using Model Updating," *Journal of Aircraft*, Vol. 55, No. 4, 2018, pp. 1551–1563. doi:https://doi.org/10.2514/1.C034684.

[12] Hodges, D. H., "Geometrically Exact, Intrinsic Theory for Dynamics of Curved and Twisted Anisotropic Beams," *AIAA Journal*, Vol. 41, No. 6, 2003, pp. 1131–1137. doi:https://doi.org/10.2514/2.2054.

[13] Wang, Z., Chen, P. C., Liu, D. D., and Mook, D. T., "Nonlinear-Aerodynamics/Nonlinear-Structure Interaction Methodology for a High-Altitude Long-Endurance Wing," *Journal of Aircraft*, Vol. 47, No. 2, 2010, pp. 556–566. doi:https://doi.org/10.2514/1.45694.

[14] Cesnik, C., and Su, W., "Nonlinear Aeroelastic Modeling and Analysis of Fully Flexible Aircraft," *46th AIAA/ASME/ASCE/AHS/ASC Structures, Structural Dynamics and Materials Conference*, AIAA, Austin, TX, 2005. doi:https://doi.org/10.2514/6.2005-2169.

[15] Artola, M., Wynn, A., and Palacios, R., "A Modal-Based Nonlinear Model Predictive Control for 3D Very Flexible Structures," Under review at *IEEE Transactions in Automatic Control*.

[16] Shearer, C. M., and Cesnik, C. E., "Nonlinear Flight Dynamics of Very Flexible Aircraft," *Journal of Aircraft*, Vol. 44, No. 5, 2007, pp. 1528–1545. doi:https://doi.org/10.2514/1.27606.

[17] Izraelevitz, J. S., Zhu, Q., and Triantafyllou, M. S., "State-Space Adaptation of Unsteady Lifting Line Theory: Twisting/Flapping Wings of Finite Span," *AIAA Journal*, Vol. 55, No. 4, 2017, pp. 1279–1294. doi:https://doi.org/10.2514/1.J055144.

[18] Brase, L. O., and Eversman, W., "Application of Transient Aerodynamics to the Structural Nonlinear Flutter Problem," *Journal of Aircraft*, Vol. 25, No. 11, 1988, pp. 1060–1068. doi:https://doi.org/10.2514/3.45703.

[19] Murua, J., Palacios, R., and Graham, J. M. R., "Applications of the Unsteady Vortex-Lattice Method in Aircraft Aeroelasticity and Flight Dynamics," *Progress in Aerospace Sciences*, Vol. 55, 2012, pp. 46 – 72. doi:https://doi.org/10.1016/j.paerosci.2012.06.001.

[20] Maraniello, S., and Palacios, R., "State-Space Realizations and Internal Balancing in Potential-Flow Aerodynamics with Arbitrary Kinematics," *AIAA Journal*, Vol. 57, No. 6, 2019, pp. 1–14. doi:https://doi.org/10.2514/1.J058153.

[21] Bock, H., and Krämer-Eis, P., "A Multiple Shooting Method for Numerical Computation of Open and Closed Loop Controls in Nonlinear Systems," *IFAC Proceedings Volumes*, Vol. 17, No. 2, 1984, pp. 411–415. doi:https://doi.org/10.1016/S1474-6670(17)61005-X.

[22] Diehl, M., Bock, H., and Schlöder, J., "A Real-Time Iteration Scheme for Nonlinear Optimization in Optimal Feedback Control," *SIAM Journal on Control and Optimization*, Vol. 43, No. 5, 2005, pp. 1714–1736. doi:https://doi.org/10.1137/S0363012902400713.

[23] Artola, M., Wynn, A., and Palacios, R., "Generalized Kelvin–Voigt Damping for Geometrically Nonlinear Beams," *AIAA Journal*, 2020. doi:https://doi.org/10.2514/1.J059767, article in advance.

[24] Hanson, A., *Visualizing quaternions*, Elsevier, 2005.

[25] del Carre, A., Muñoz-Simón, A., Goizueta, N., and Palacios, R., "SHARPy: A Dynamic Aeroelastic Simulation Toolbox for Very Flexible Aircraft and Wind Turbines," *Journal of Open Source Software*, Vol. 4, No. 44, 2019, p. 1885. doi: https://doi.org/10.21105/joss.01885.

[26] del Carre, A., and Palacios, R., "Efficient Time-Domain Simulations in Nonlinear Aeroelasticity," *AIAA Scitech 2019 Forum*, San Diego, CA, 2019. doi:https://doi.org/10.2514/6.2019-2038.

[27] del Carre, A., Teixeira, P. C., Palacios, R., and Cesnik, C. E. S., "Nonlinear Response of a Very Flexible Aircraft Under Lateral Gust," *International Forum on Aeroelasticity and Structural Dynamics - IFASD 2019-090*, 2019.

[28] Simpson, R. J. S., Palacios, R., and Murua, J., "Induced-Drag Calculations in the Unsteady Vortex Lattice Method," *AIAA Journal*, Vol. 51, No. 7, 2013, pp. 1775–1779. doi:https://doi.org/10.2514/1.j052136.

[29] Lambert, T., and Dimitriadis, G., "Induced Drag Calculations with the Unsteady Vortex Lattice Method for Cambered Wings," *AIAA Journal*, Vol. 55, No. 2, 2016, pp. 668–672. doi:https://doi.org/10.2514/1.j055135.

[30] Palacios, R., and Epureanu, B., "An Intrinsic Description of the Nonlinear Aeroelasticity of Very Flexible Wings," *52nd AIAA/ASME/ASCE/AHS/ASC Structures, Structural Dynamics and Materials Conference*, Denver, Colorado, 2011. doi: https://doi.org/10.2514/6.2011-1917.

[31] Palacios, R., "Nonlinear Normal Modes in an Intrinsic Theory of Anisotropic Beams," *Journal of Sound and Vibration*, Vol. 330, No. 8, 2011, pp. 1772–1792. doi:https://doi.org/10.1016/j.jsv.2010.10.023.

[32] Wynn, A., Wang, Y., Palacios, R., and Goulart, P. J., "An Energy-Preserving Description of Nonlinear Beam Vibrations in Modal Coordinates," *Journal of Sound and Vibration*, Vol. 332, No. 21, 2013, pp. 5543 – 5558. doi:https://doi.org/10.1016/j.jsv.2013.05.021.

[33] Roesler, B. T., and Epps, B. P., "Discretization Requirements for Vortex Lattice Methods to Match Unsteady Aerodynamics Theory," *AIAA Journal*, Vol. 56, No. 6, 2018, pp. 2478–2483. doi:https://doi.org/10.2514/1.J056400.

[34] Gallivan, K. A., Grimme, E. J., and Van Dooren, P. M., "Model Reduction of Large-Scale Systems Rational Krylov Versus Balancing Techniques," *Error Control and Adaptivity in Scientific Computing*, 1999, pp. 177–190. doi:https://doi.org/10.1007/978-94-011-4647-0_9.

[35] Murua, J., Palacios, R., and Graham, J. M. R., "Open-Loop Stability and Closed-Loop Gust Alleviation on Flexible Aircraft Including Wake Modeling," *53rd AIAA/ASME/ASCE/AHS/ASC Structures, Structural Dynamics and Materials Conference*, Honolulu, HI, 2012. doi:https://doi.org/10.2514/6.2012-1484.

[36] del Carre, A., and Palacios, R., "Simulation and Optimization of Takeoff Maneuvers of Very Flexible Aircraft," *Journal of Aircraft*, Vol. 57, No. 6, 2020, pp. 1097–1110. doi:10.2514/1.C035901.

[37] Antoulas, A. C., *Approximation of Large-Scale Dynamical Systems*, 1st ed., SIAM - Advances in Design and Control, 2005.

[38] Arnoldi, W. E., "The Principle of Minimized Iterations in the Solution of the Matrix Eigenvalue Problem," *Quarterly of Applied Mathematics*, Vol. 9, No. 1, 1951, pp. 17–29. doi:https://doi.org/10.1090/qam/42792.

[39] Gugercin, S., "Projection Methods for Model Reduction of Large-Scale Dynamical Systems," Ph.D. thesis, Rice University, 2003.

[40] Gallivan, K., Vandendorpe, A., and Van Dooren, P., "Sylvester Equations and Projection-Based Model Reduction," *Journal of Computational and Applied Mathematics*, Vol. 162, No. 1, 2004, pp. 213–229. doi:https://doi.org/10.1016/j.cam.2003.08.026.

[41] Glover, K., "All Optimal Hankel-Norm Approximations of Linear Multivariable Systems and Their L_∞ -Error Bounds†," *International Journal of Control*, Vol. 39, No. 6, 1984, pp. 1115–1193. doi:https://doi.org/10.1080/00207178408933239.

[42] Nocedal, J., and Wright, S. J., *Numerical Optimization*, 2nd ed., Springer, 2006.

[43] Cao, Y., Li, S., Petzold, L., and Serban, R., "Adjoint Sensitivity Analysis for Differential-Algebraic Equations: the Adjoint DAE System and its Numerical Solution," *Journal of Scientific Computing*, Vol. 24, No. 3, 2003, pp. 1076–1089. doi: https://doi.org/10.1016/S0377-0427(02)00528-9.

[44] Artola, M., Goizueta, N., Wynn, A., and Palacios, R., "Modal-Based Nonlinear Estimation and Control for Highly Flexible Aeroelastic Systems," *AIAA SciTech 2020 Forum*, Orlando, FL, 2020. doi:https://doi.org/10.2514/6.2020-1192.

[45] Artola, M., Wynn, A., and Palacios, R., "A Nonlinear Modal-Based Framework for Low Computational Cost Optimal Control of 3D Very Flexible Structures," *2019 European Control Conference*, Naples, Italy, 2019. doi:https://doi.org/10.23919/ECC.2019.8796151.

[46] Palacios, R., Murua, J., and Cook, R., "Structural and Aerodynamic Models in Nonlinear Flight Dynamics of Very Flexible Aircraft," *AIAA Journal*, Vol. 48, No. 11, 2010, pp. 2648–2659. doi:https://doi.org/10.2514/1.J050513.

[47] Avin, O., Drachinsky, A., Ben Shmuel, Y., and Raveh, D. E., "An Experimental Benchmark of a Very Flexible Wing," *AIAA SciTech Forum*, 2021.

[48] Goizueta, N., Wynn, A., Palacios, R., Drachinksy, A., and Raveh, D. E., "Flutter Predictions for very Flexible Wing Wind Tunnel Test," *AIAA SciTech Forum*, 2021.